ELEMENTA
Science of the Anthropocene

Buesseler, KO, et al. 2020. High-resolution spatial and temporal measurements of particulate organic carbon flux using thorium-234 in the northeast Pacific Ocean during the EXport Processes in the Ocean from RemoTe Sensing field campaign. *Elem Sci Anth*, 8: 1. DOI: https://doi.org/10.1525/elementa.2020.030

RESEARCH ARTICLE

High-resolution spatial and temporal measurements of particulate organic carbon flux using thorium-234 in the northeast Pacific Ocean during the EXport Processes in the Ocean from RemoTe Sensing field campaign

Ken O. Buesseler[1,*], Claudia R. Benitez-Nelson[2], Montserrat Roca-Martí[1], Abigale M. Wyatt[3], Laure Resplandy[3], Samantha J. Clevenger[1,4], Jessica A. Drysdale[1], Margaret L. Estapa[5,6], Steven Pike[1], and Blaire P. Umhau[2]

The EXport Processes in the Ocean from RemoTe Sensing (EXPORTS) program of National Aeronautics and Space Administration focuses on linking remotely sensed properties from satellites to the mechanisms that control the transfer of carbon from surface waters to depth. Here, the naturally occurring radionuclide thorium-234 was used as a tracer of sinking particle flux. More than 950 ^{234}Th measurements were made during August–September 2018 at Ocean Station Papa in the northeast Pacific Ocean. High-resolution vertical sampling enabled observations of the spatial and temporal evolution of particle flux in Lagrangian fashion. Thorium-234 profiles were remarkably consistent, with steady-state (SS) ^{234}Th fluxes reaching 1,450 $\pm$ 300 dpm m^{-2} d^{-1} at 100 m. Nonetheless, ^{234}Th increased by 6%–10% in the upper 60 m during the cruise, leading to consideration of a non-steady-state (NSS) model and/or horizontal transport, with NSS having the largest impact by decreasing SS ^{234}Th fluxes by 30%. Below 100 m, NSS and SS models overlapped. Particulate organic carbon (POC)/^{234}Th ratios decreased with depth in small (1–5 μm) and mid-sized (5–51 μm) particles, while large particle (>51 μm) ratios remained relatively constant, likely influenced by swimmer contamination. Using an average SS and NSS ^{234}Th flux and the POC/^{234}Th ratio of mid-sized particles, we determined a best estimate of POC flux. Maximum POC flux was 5.5 $\pm$ 1.7 mmol C m^{-2} d^{-1} at 50 m, decreasing by 70% at the base of the primary production zone (117 m). These results support earlier studies that this site is characterized by a modest biological carbon pump, with an export efficiency of 13% $\pm$ 5% (POC flux/net primary production at 120 m) and 39% flux attenuation in the subsequent 100 m (POC flux 220 m/POC flux 120m). This work sets the foundation for understanding controls on the biological carbon pump during this EXPORTS campaign.

Keywords: Thorium-234, Ocean Station Papa, Particulate organic carbon flux, EXPORTS, Biological carbon pump

1. Introduction

Marine ecosystems are of fundamental importance with regard to their capacity to influence the storage, transformation, and fate of carbon (C) and associated elements in the Earth's biosphere (Falkowski et al., 2000; Sarmiento and Gruber, 2002; Chavez et al., 2011; Doney et al., 2012). Yet the mechanisms that influence the movement of fixed C from well-lit surface waters to the ocean's interior remain elusive (Siegel et al., 2016). Even small changes in the magnitude of downward transport of C in the ocean, or export, in global Earth system models can have major impacts on ocean C sequestration and thus on predicted atmospheric CO_2 concentrations (Kwon et al., 2009). Subtle differences in export further influence

[1] Department of Marine Chemistry & Geochemistry, Woods Hole Oceanographic Institution, Woods Hole, Massachusetts, United States

[2] School of the Earth, Ocean and Environment, University of South Carolina, Columbia, South Carolina, United States

[3] Department of Geosciences, Princeton University, Princeton, New Jersey, United States

[4] Department of Earth, Atmospheric and Planetary Sciences, Massachusetts Institute of Technology, Cambridge, Massachusetts, United States

[5] Geosciences Department, Skidmore College, Saratoga Springs, New York, United States

[6] Darling Marine Center, School of Marine Sciences, University of Maine, Walpole, Maine, United States

* Corresponding author:
Email: kbuesseler@whoi.edu

Downloaded from http://online.ucpress.edu/elementa/article-pdf/8/1/030/468942/elementa.2020.030.pdf by guest on 11 July 2024

biological food webs with regard to biodiversity and fisheries abundance (e.g., Beaugrand et al., 2010) as well as the fate of other biologically associated and particle-scavenged elements, such as heavy metals and organic contaminants (Shine et al., 1995; Gustafsson et al., 1997).

The primary goal of the EXport Processes in the Ocean from RemoTe Sensing (EXPORTS) program of the National Aeronautics and Space Administration is to develop a predictive understanding of the export and fate of fixed C from global ocean primary production (Siegel et al., 2016). Inherent in these models is the need to reduce uncertainties in C export estimates and to develop constructs that facilitate future C export estimates across a variety of spatial and temporal scales. As such, critical components of the EXPORTS Program are quantitative measurements of sinking particle fluxes and their attenuation versus depth at scales similar to the physical and biological processes that influence fixed C export.

Measuring particle export is confounded by high temporal and spatial variability on vertical scales of <10–100 m, horizontal scales of <3–5 km, and time scales of days to weeks (Benitez-Nelson and McGillicuddy, 2008; Estapa et al., 2015; Stukel et al., 2017). A mechanistic understanding of export processes has been further hampered by the few methods that are able to capture the non-steady-state nature of ocean C flux and its inherent patchiness. These methods are either direct measurement of C fluxes using a variety of sediment trap types (McDonnell et al., 2015), indirect methods such as using radioactive tracers (Buesseler et al., 1998; Verdeny et al., 2009; Haskell et al., 2015) or geochemical mass balance (e.g., Hamme et al., 2019). All these approaches sample over dissimilar spatial and temporal scales and with different operational biases (Burd et al., 2010; Estapa et al., 2015).

Here, we use the radioactive tracer, thorium-234 (half-life, $t_{½} = 24.1$ days) to quantify the spatio-temporal variability in particle flux from the well-lit surface layer (euphotic zone, Ez) and its attenuation with depth in the twilight zone below. ^{234}Th is produced by the radioactive decay of uranium-238 ($t_{½} = 4.47 \times 10^9$ years) in the water column. As ^{234}Th is highly particle reactive, it is rapidly adsorbed onto sinking particles and released back into the dissolved phase when those particles are remineralized. The disequilibrium from its soluble conservative parent, ^{238}U, provides quantitative information on where particle export (^{234}Th deficiency due to net removal) and remineralization (^{234}Th excess due to solubilization or fragmentation, i.e., conversion of sinking into nonsinking phases) occur in the water column (e.g., Buesseler et al., 1992). As such, ^{234}Th provides rates of downward C fluxes over the smaller vertical and spatial scales required to understand processes that regulate water column export and C attenuation in a dynamic marine system.

This work was part of the EXPORTS field campaign that included satellite remote sensing, autonomous platforms, and observations from survey and process ships to gather key measurements of rates, stocks, and physical and biological processes, including primary production and particle flux (Siegel et al., 2020). We present an extensive set of three-dimensional time-series profiles of total ^{234}Th ($n =$ 61) that were collected in the late summer in the northeast subarctic Pacific near Ocean Station Papa (Station P). This high spatial and temporal resolution allowed an assessment of steady-state and non-steady-state particulate organic C (POC) flux throughout the upper water column using POC/^{234}Th ratios from filtered particles collected using in situ pumps. These are among the earliest EXPORTS results and thus provide a foundation on which to build subsequent assessments of additional C cycle pathways and mechanisms and support EXPORTS goals of obtaining a predictive understanding of the export, fate, and impacts of global ocean net primary production (NPP).

2. Study Site

This first EXPORTS study was conducted near the time-series Station P in the northeast subarctic Pacific (50°N, 145°W) from August 9 to September 13, 2018. Station P was established in 1949 and maintains one of the oldest oceanic time-series programs. This high-nutrient low-chlorophyll region is characterized by a modest spring bloom that typically occurs in March and April and is comprised of a mixture of coccolithophores and diatoms (Boyd and Harrison, 1999; Fassbender et al., 2016). Prior to EXPORTS, particle fluxes were measured for more than two decades using deep-ocean sediment traps (Timothy et al., 2013). In addition, drifting trap arrays were deployed from 50 to 1,000 m during the period of 1987–1998 (Wong et al., 2002). Also important are prior studies at Station P that included water column ^{234}Th measurements for determining sinking C fluxes (Charette et al., 1999; Kawakami et al., 2010; Mackinson et al., 2015).

The water column samples discussed here were collected onboard the R/V *Sally Ride*, which conducted a series of small-scale (approximately 900 km^2) and large-scale (approximately 7,700 km^2) surveys, from 49.5 to 50.9°N and 144.5 to 145.8°W, over a period of 28 days (**Figure 1**). These surveys were centered on a drifting Lagrangian float deployed at approximately 100 m, just below the base of the winter mixed layer and near the 0.1% penetration depth of photosynthetic active radiation (PAR; Siegel et al., 2020). Surveys were conducted over 3 time periods or "epochs," each lasting 7–8 days. Epochs were set largely by the logistical constraints of sampling and the assumption that surface-derived particles would take 5–10 days to reach 500 m at sinking rates of 50–100 m d^{-1}, which allows surface events to be tied to particle fluxes at depth within each epoch. During an epoch, total ^{234}Th samples were collected from approximately 20 water column profiles using Niskin bottles attached to a rosette with a Sea-Bird 911 system configured with 2 SBE temperature and salinity sensors, 1 SBE 43 oxygen sensor, and 1 Digiquartz pressure sensor. Connected to the Sea-Bird 911 system were a WET Labs C-Star 650-nm beam transmissometer, a Biospherical QSE scalar PAR sensor, and a WET Labs FLBBRTD combination chlorophyll fluorometer and backscatter (700 nm) sensor, which we used to define the Ez. Each epoch also included the collection of size-fractioned particles from large volume in situ pumps ($n = 12$ casts in total).

Downloaded from http://online.ucpress.edu/elementa/article-pdf/8/1/030/468942/elementa.2020.030.pdf by guest on 11 July 2024

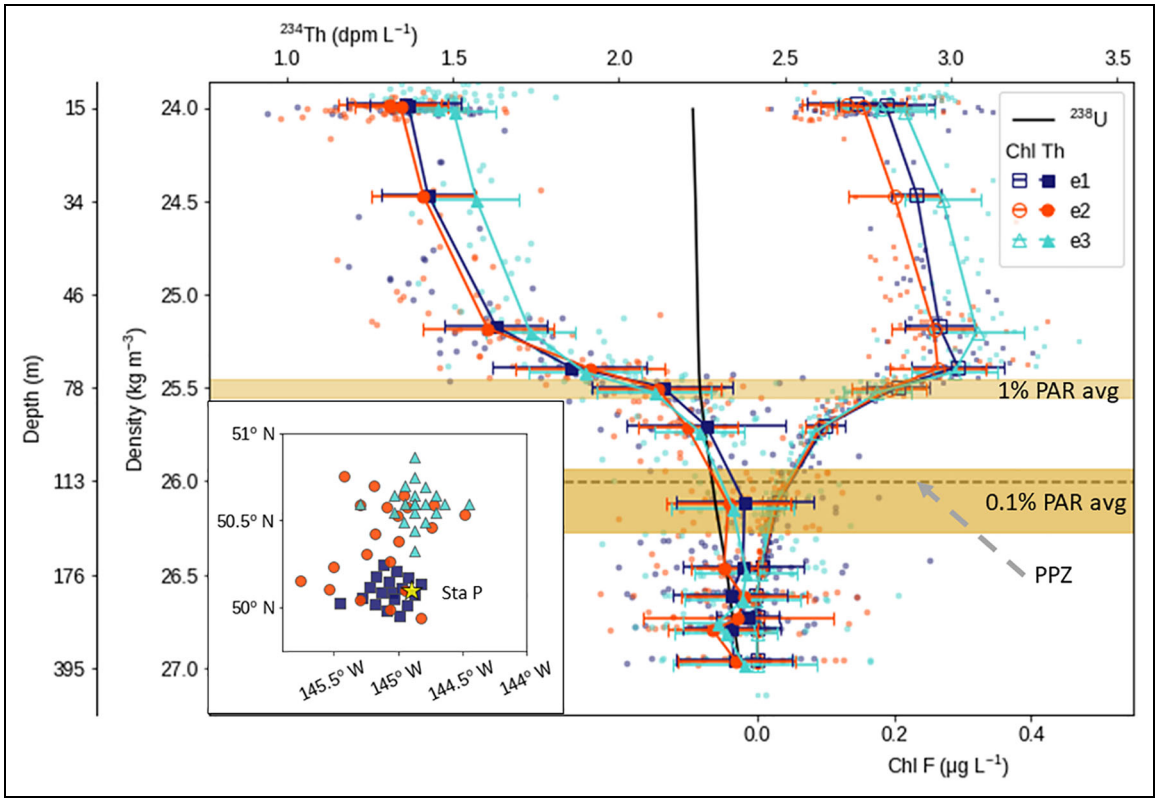

Figure 1. Thorium-234 and chlorophyll versus density. Thorium-234 activity (dpm L^{-1}, upper *x*-axis) and chlorophyll fluorescence (µg L^{-1}, lower offset *x*-axis) versus density are denoted by circle and square markers, respectively, colored by epoch. Epoch average is shown in larger symbols with the error bar denoting one standard deviation. Uranium-238 activity (dpm L^{-1}) is shown by the vertical black line. Yellow bars are the cruise-average 1% photosynthetic active radiation (PAR; 79 ± 6 m) and 0.1% PAR (118 ± 9 m) regions. The dashed gray line is the bottom of the primary production zone (PPZ = 117 ± 5 m). Equivalent depths are shown on secondary *y*-axis. Map insert shows spatial location of sampling relative to Station P. DOI: https://doi.org/10.1525/elementa.2020.030.f1

3. Methods

3.1. Total thorium-234

Total ^{234}Th sampling and analyses were similar to those described in the study of Buesseler et al. (2001) using a smaller volume of 2-L versus 4-L samples. This method is based on the formation of a manganese dioxide precipitate, which preferentially scavenges ^{234}Th, leaving ^{238}U in the dissolved phase. Unfiltered seawater was collected from 10-L Niskin bottles at 61 stations, each with 13–18 sample depths over the upper 500 m. Samples were immediately acidified to pH 1 with concentrated HNO_3 acid and a 1-mL aliquot of ^{230}Th (approximately 50 disintegrations per minute, dpm g^{-1}) added for use as a yield monitor (Pike et al., 2005). Samples were allowed to equilibrate for 6–8 h and then adjusted to a pH of approximately 8.5 using concentrated NH_4OH. Reagents $KMnO_4$ and $MnCl_2$ were added to precipitate the Mn oxide. Samples were allowed to stand for approximately 8 h, filtered onto 25-mm diameter quartz microfiber filters (QMA), and dried at 60 °C.

Once dry, the filters were mounted under Mylar and two layers of aluminum foil and counted on 1 of the 6 anticoincidence, 5-sample, low-level Risø β counters. Each β counter was surrounded by 8 cm of lead, resulting in extremely low background counts (average = 0.26 counts per minute, cpm). Samples were typically counted twice at sea with counting errors of <3%, and the average value was used after appropriate decay and ingrowth corrections. Close examination of decay curves and counting errors allowed us to identify outliers in cases where first and second counts disagreed by more than 0.2 dpm L^{-1}. Samples were recounted >6 months after collection for background activity (approximately 0.48 ± 0.24 cpm) stemming from other naturally occurring β-emitting radionuclides that are included in the precipitate (most likely radium daughters; Benitez-Nelson et al., 2001b). Cross calibration and counting efficiencies of β detectors were assessed 2–3 times during and after the cruises using ^{238}U standards that have an activity similar to the measured samples. Standards were rotated and counted on each of the 5 positions for the 6 different Risø detectors. The detector efficiencies varied by <2% in 24 of the 30 detectors and by <5% in the remaining detectors. ^{234}Th values are reported in activity units (dpm L^{-1}) and are provided in the SeaBASS Data Repository (https://seabass.gsfc.nasa.gov/archive/WHOI/buesseler/EXPORTS/EXPORTSNP/archive/).

All total ^{234}Th activities were corrected for the overall efficiency of the Mn oxide precipitation method as determined using ^{230}Th as a yield monitor. Recovery of ^{230}Th was conducted after the final background β count using procedures detailed in the study of Pike et al. (2005),

Downloaded from http://online.ucpress.edu/elementa/article-pdf/8/1/030/468942/elementa.2020.030.pdf by guest on 11 July 2024

modified to no longer use an ion-exchange column to reduce Mn interferences. Precipitates were dissolved in a nitric acid and hydrogen peroxide solution, and a known amount of ^{229}Th was added to each sample. The ^{230}Th/^{229}Th ratio was then analyzed by inductively coupled plasma mass spectrometry, thus allowing for the determination of ^{230}Th present in each sample and correction for Th loss during processing. Recoveries averaged 88 $\pm$ 9%. Samples with recoveries <40% were excluded from the data set (n = 2). For samples with apparent recoveries >100% (n = 18, average recovery = 107.3 $\pm$ 8.5%), recoveries were fixed at 100%, and sample errors were increased to 5% to calculate final results. Variations in the amount of ^{230}Th added on different casts required cast-by-cast consideration of final recoveries. The 10 samples collected at depth (2 casts of n = 5 at 3,000 m) confirmed secular equilibrium with ^{238}U (2.41 dpm L^{-1}), with average ^{234}Th activities of 2.40 $\pm$ 0.14 and 2.42 $\pm$ 0.15 dpm L^{-1}, measured early and late in the cruise, respectively. Errors on individual ^{234}Th activities were propagated from the initial and final counts as well as from the error on the ^{230}Th-derived yield.

3.2. Size-fractionated particles collected using in situ pumps

Size-fractionated particles were collected by Large Volume Water Transfer System battery-powered in situ pumps (McLane Industries) that were modified to accommodate two 142-mm diameter mini-MULVFS (Multiple Unit Large Volume Filtration System) filter holders (Lam et al., 2015). Size-fractionated particles for ^{234}Th and other isotope, element, and compound analyses were collected using a single flow path through a 3-stage filter holder. Pumps were deployed on a total of 12 casts at 50 m and at the depths of the sediment traps: 100, 150, 200, 330, and 500 m $\pm$ 5 m (Estapa et al., 2020). A pressure sensor attached to the deepest pump confirmed depths, which can vary depending on the wire angle. Filtration volumes ranged from 700 to 1,500 L for 4–5 hours at an initial flow rate of 8 L min^{-1}. Filter holders were loaded with 51- and 5-µm pore size acid-cleaned Nitex screens followed by a 1-µm pore size precombusted QMA filter. Sampling at these 6 depths at 12 stations generated 72 samples for each of the 3 size classes (1–5, 5–51, and >51 µm). Once per epoch a filter holder containing a full set of filters, but without any active water pumping, was mounted on the deepest in situ pump at 500 m to obtain process (or dipped) blanks (Lam et al., 2015). These blanks were processed in the same manner as the samples. Size-fractionated particles were analyzed for ^{234}Th, particulate carbon (PC) and particulate inorganic carbon (PIC), and other analytes including particulate nitrogen, biogenic silica, phosphorus, pigments, ^{210}Po/^{210}Pb, barium, Ba isotopes, and other organic compounds. Results for these other analytes will be presented elsewhere. During 3 pump deployments, additional samples (n = 5) for the smallest particle size class (1–5 µm) were collected at 20, 85, and 320 m by deploying extra in situ pumps. These samples were collected using a single flow path through a mini-MULVFS filter holder loaded with 51- and 6-µm pore size Nitex screens followed by paired QMA filters and paired 0.3-µm pore size GF75 filters.

Particles were gently rinsed off the Nitex screens onto a 25-mm diameter 1.2-µm pore size silver (Ag) filters using 1-µm filtered seawater collected at depths from 330 to 500 m that was stored refrigerated at 4 °C and collected once per epoch. At these depths, dissolved organic C concentrations were approximately 45 µM (Bif and Hansell, 2019), and appropriate C filter processing blanks were assessed. At 9 stations, the entire screens were rinsed, whereas at 3 stations, the screens were cut in half using a rotary blade to allow for analysis of other analytes according to the GEOTRACES sample-handling protocol (Cutter et al., 2017). QMA filters were subsampled with punches of 21–26 mm diameter for ^{234}Th, PC, and PIC, as particle distribution has been shown to be uniform across the filter (Maiti et al., 2012). All filters were dried in a 60 °C oven, β counted at sea for ^{234}Th activities, and recounted 6 months later onshore for backgrounds. After counting, screen samples that had been rinsed onto Ag filters were split by weight (Lamborg et al., 2008), and one-third of each sample was analyzed for PC and PIC. PC was analyzed using high-temperature combustion on a Thermo Electron FlashEA 1112 C/N analyzer at the WHOI Nutrient Analytical Facility. PIC was determined by coulometric analysis of CO_2 after acidification with phosphoric acid (Honjo et al., 1995).

The average of all process blanks was subtracted from total ^{234}Th, PC, and PIC measurements. Process blanks for ^{234}Th and PC were <2% of total ^{234}Th and PC (Ag filters: 0.15 $\pm$ 0.11 dpm ^{234}Th, 1/3 Ag filters: 0.17 $\pm$ 0.28 µmol C; QMA punches: 0.13 $\pm$ 0.06 dpm ^{234}Th, 0.15 $\pm$ 0.21 µmol C). In contrast, PIC concentrations were quite low (<3% of total C). Therefore, PIC process blanks were relatively higher, accounting for 82% of the measured PIC on 1/3 Ag filters (0.47 $\pm$ 0.03 µmol C) and 42% of PIC on the QMA punches (0.23 $\pm$ 0.01 µmol C). Three replicate punches from a 50 and a 500-m sample were analyzed for PC and PIC, obtaining a standard deviation of <5% for both analyses. POC concentrations were obtained from the difference between blank-corrected PC and PIC results. Data for POC have associated uncertainties derived from these blank corrections and weighing errors of the analytical balance used for splitting the Ag filters. Particulate ^{234}Th data have an associated uncertainty from counting and blank corrections. All size-fractionated particle data from the 2018 EXPORTS expedition are found in the SeaBASS Data Repository (https://seabass.gsfc.nasa.gov/archive/WHOI/buesseler/EXPORTS/EXPORTSNP/archive/).

Swimmers (nondetrital zooplankton) observed by the naked eye were picked from the 51-µm screens. However, complete removal of swimmers was not always possible due to the high abundance of tiny copepods (<0.5 mm) that were difficult to remove without eliminating a significant amount of the passive sinking particles. Subsequent photographic analysis confirmed the presence of larger zooplankton on some of the Ag filters, particularly at depths >100 m. Seven (of 72) samples were identified as outliers based on high POC/^{234}Th (hereafter referred to as C/Th) values following the interquartile method by Tukey

Downloaded from http://online.ucpress.edu/elementa/article-pdf/8/1/030/468942/elementa.2020.030.pdf by guest on 11 July 2024

(1977). Outliers were defined by measurements with values greater than the third quartile by more than 1.5 times the interquartile range (i.e., third quartile–first quartile) and were removed from subsequent >51 μm data analysis. The remaining large particle data were characterized by a normal C/Th distribution, as observed in the other two pump-derived size classes.

4. Results

4.1. Ancillary data

As part of this study, we derived chlorophyll (chl) concentrations from fluorescence on the same casts as those where total ^{234}Th was sampled. These data are shown in **Figure 1**, with the *x*-axis shifted to the right for clarity. Chlorophyll was quantified from the raw conductivity, temperature, and depth (CTD) fluorescence sensor data (CTD ChlF, measured in volts, V) using chl (μg L^{-1}) = [raw CTD ChlF (V) – dark value (V)]/[slope of calibration curve (V/(μg L^{-1})] with a calibration slope = 0.64 ± 0.01 V/(μg L^{-1}) and dark value = 0.0870 ± 0.0009 V, as derived by the EXPORTS calibration team.

Previous work has shown that chl can be used to define the base of the sunlit Ez. Using CTD fluorescence sensor data, Owens et al. (2015) defined this base of the "primary production zone" (PPZ) as the depth at which the signal from in situ fluorescence dropped to 10% of the maximum above that depth (after correction for sensor background signal). On our CTD casts, the PPZ (117 ± 5 m) overlapped with the zone of net ^{234}Th removal (^{234}Th/^{238}U < 1.0; **Figure 1**) similar to many previous studies (e.g., Buesseler et al., 2020). PAR was also measured as an indicator of the Ez depth and is shown in **Figure 1**. The depth where ^{234}Th reaches equilibrium fell between the depth of 1% ($Ez_{1.0}$ = 79 ± 6 m) and 0.1% PAR ($Ez_{0.1}$ = 118 ± 9 m).

4.2. Thorium-234 activity profiles

The results of all 760 analyses of total ^{234}Th are provided in **Figure 1**, with the average (± standard deviation) from all three epochs shown versus depth and density. This depiction allows for more careful alignment of individual vertical profiles, given depth variability in physical properties. Average ^{234}Th and ^{238}U activities are also provided in **Table 1**, with individual data available in SeaBASS and in Table S1 (along with the calculated ^{234}Th and POC fluxes discussed in the following sections). Salinity varied minimally throughout the sampling periods, mainly increasing with greater depth, resulting in ^{238}U activities ranging from 2.22 dpm L^{-1} at the surface to 2.36 dpm L^{-1} by 500 m. Overall, ^{234}Th activities averaged 1.37 ± 0.15 dpm L^{-1} in the upper 10 m and reached equilibrium with ^{238}U around a density of 25.75 kg m^{-3} (about 80–90 m). Below this depth, average ^{234}Th activities exceeded that of ^{238}U, before returning to equilibrium at a density of 26.5 kg m^{-3} (about 180 m).

The spatio-temporal variability of ^{234}Th activity was fairly consistent per epoch, with a cruise-average standard deviation of 0.17 dpm L^{-1} per depth (**Figure 1**), roughly 6%–11% of the mean ^{234}Th activity throughout the water column (**Table 1**). Mean ^{234}Th activities in Epochs 1 and 2 were similar. In contrast, they significantly increased from Epoch 1 to Epoch 3 by 6%–10% at depths shallower than 60 m or densities less than 25.0 kg m^{-3} (Figure S1 and **Table 1**). However, the overall shape of the vertical profiles did not change (**Figure 1**).

4.3. Thorium-234 flux modeling

The flux of ^{234}Th on sinking particles may be determined using a general thorium activity balance calculated using vertically integrated ^{234}Th activities above a given depth horizon:

$$\frac{d(^{234}\mathrm{Th})}{dt} = \lambda(^{238}\mathrm{U} - ^{234}\mathrm{Th}) - ^{234}\mathrm{Th}E + V, \quad (1)$$

where $\frac{d(^{234}Th)}{dt}$ is the change in the vertically integrated ^{234}Th activity (dpm m^{-2}) over a given depth interval (*z*) over time, t, λ is the radioactive decay constant of ^{234}Th determined from the half-life of ^{234}Th, 0.02876 d^{-1}, *V* is the sum of physical advection and diffusion processes, and ^{234}Th*E* is the thorium flux associated with particle export (dpm m^{-2} d^{-1}) from the integrated depth zone of interest. ^{238}U activities (dpm L^{-1}) at each depth are determined using salinity (*S*) as measured using the CTD and Equation 2 (Owens et al., 2011):

$$^{238}\mathrm{U} = 0.0786 \times S - 0.315. \quad (2)$$

All fluxes of ^{234}Th were driven by the difference in vertically integrated ^{234}Th versus ^{238}U activities. As such, this difference became smaller with increasing depth, as ^{234}Th approached equilibrium with ^{238}U and ^{234}Th-derived flux errors increased with depth for a given profile (**Table 1**). Sampling depth intervals provided additional error as depth sampling increased to ≥50 m below 150 m. This wider depth resolution limited definition of the integrated ^{234}Th/^{238}U ratio (**Table 1**).

4.3.1. Steady-state model

Given the small spatial variability, a 1-dimensional steady-state (SS) model $\left(\frac{d(^{234}Th)}{dt} = 0; V = 0\right)$ was used to determine ^{234}Th-derived export fluxes (Savoye et al., 2006). Integrating the activity balance from the surface to depth (*D*) allowed a calculation of the net ^{234}Th export over a specific depth zone in dpm m^{-2} d^{-1} (Equation 3).

$$^{234}\mathrm{Th}E_{SS} = \int_{z=D}^{0} \lambda(^{238}\mathrm{U} - ^{234}\mathrm{Th}). \quad (3)$$

We computed a SS export flux for each individual ^{234}Th profile (Table S1) and then computed a cruise average for each depth bin (**Table 1**). The uncertainty for the cruise average was determined using the standard deviation across all ^{234}Th flux SS estimates. No errors were assigned to ^{238}U profiles, as variability in ^{238}U versus salinity has been observed to be low in the vast majority of open ocean data, with the exception of a few locations where rivers, ice, or coastal and low oxygen conditions result in local, nonconservative behavior of ^{238}U (e.g., Owens et al., 2011; Xie et al., 2020).

Downloaded from http://online.ucpress.edu/elementa/article-pdf/8/1/030/468942/elementa.2020.030.pdf by guest on 11 July 2024

Table 1. ^{234}Th activities by epoch and cruise-average ^{234}Th fluxes binned by depth. DOI: https://doi.org/10.1525/elementa.2020.030.t1

		^{234}Th Activity (dpm L^{-1})											^{238}U Activity (dpm L^{-1})	^{234}Th Flux (dpm m^{-2} d^{-1})			
		Epoch 1			Epoch 2			Epoch 3			Cruise		Cruise	Cruise SS[d]		Cruise NSS[e]	
Avg. Depth (m)[a]	Range (m)[b]	Average	*SD*[c]	*n*	Average	*SD*[c]	*n*	Average	*SD*[c]	*n*	Average	*SD*[c]	Average	Average	Uncert	Average	Uncert
5		1.35	0.17	18	1.31	0.16	21	1.46	0.09	19	1.37	0.15	2.22	324	80	221	120
20	15–24	1.37	0.12	17	1.34	0.14	21	1.50	0.13	16	1.40	0.14	2.22	666	145	445	195
35	25–42	1.43	0.14	14	1.41	0.16	22	1.57	0.13	23	1.48	0.16	2.23	964	181	637	254
50	45–56	1.63	0.15	18	1.61	0.20	21	1.73	0.13	19	1.66	0.17	2.24	1,276	201	789	307
65	59–69	1.85	0.23	12	1.91	0.22	14	1.90	0.17	17	1.89	0.20	2.24	1,407	254	908	386
80	75–83	2.13	0.21	17	2.12	0.19	21	2.11	0.17	21	2.12	0.19	2.25	1,444	279	997	469
100	94–109	2.26	0.24	20	2.21	0.15	23	2.24	0.13	20	2.24	0.18	2.26	1,452	304	1,024	545
120	110–130	2.38	0.21	34	2.33	0.19	40	2.34	0.18	41	2.35	0.19	2.29	1,428	365	1,026	672
150	145–151	2.37	0.18	18	2.32	0.10	22	2.38	0.15	20	2.36	0.15	2.33	1,384	422	941	861
200	194–222	2.34	0.17	22	2.38	0.19	23	2.37	0.17	22	2.36	0.18	2.34	1,283	585	774	1,263
280	249–314	2.38	0.09	14	2.36	0.29	6	2.30	0.11	6	2.36	0.16	2.34	1,192	447	1,100	1,382
330	328–334	2.34	0.15	17	2.28	0.14	21	2.32	0.15	20	2.31	0.14	2.35	1,464	885	1,270	1,961
500	498–503	2.35	0.17	12	2.35	0.18	14	2.38	0.22	13	2.36	0.19	2.36	1,527	1,119	1,116	2,437

Abbreviation: Uncert = uncertainity.

[a]Average sample depth in the bin.

[b]Depth range of the samples included in the bin.

[c]Standard deviation.

[d]Cruise-average steady-state (SS) ^{234}Th fluxes were calculated from all the SS ^{234}Th fluxes computed for each station. The uncertainty corresponds to the standard deviation across all of the SS ^{234}Th flux estimates.

[e]Non-steady-state (NSS) ^{234}Th fluxes were calculated from the depth-averaged ^{234}Th activities of Epochs 1 and 3 following Equation 4. The uncertainty was calculated by propagating the standard deviations of ^{234}Th activity from Epochs 1 and 3 through Equation 4 (see Section 4.5).

Downloaded from http://online.ucpress.edu/elementa/article-pdf/8/1/030/468942/elementa.2020.030.pdf by guest on 11 July 2024

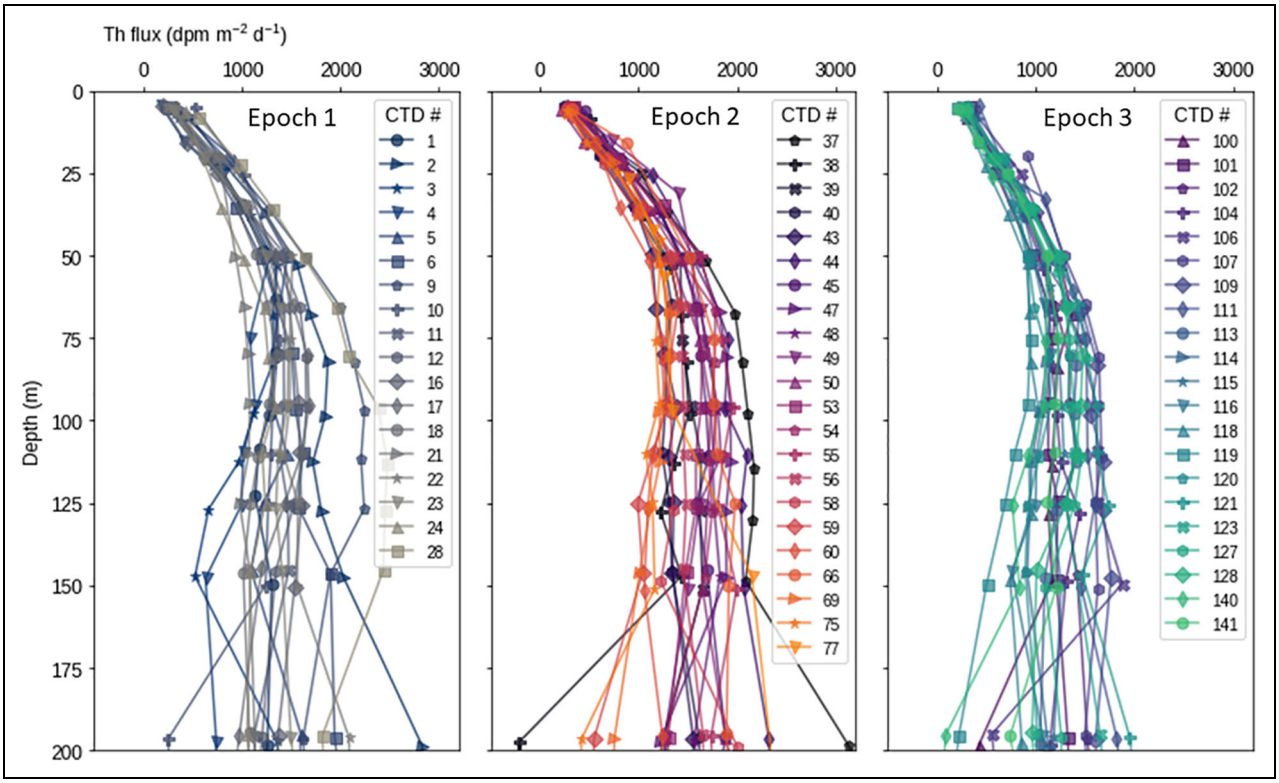

Figure 2. Thorium flux versus depth. Thorium flux (dpm m^{-2} d^{-1}) versus depth for each epoch calculated per profile using the steady-state model and colored by cast number. DOI: https://doi.org/10.1525/elementa.2020.030.f2

Fluxes of ^{234}Th increased with a similar slope throughout the upper 50 m at all stations, from an average of 324 ± 80 dpm m^{-2} d^{-1} in the upper 10 m to 1,450 ± 300 dpm m^{-2} d^{-1} by 80–100 m for the SS model (**Figure 2**). The highest ^{234}Th-derived SS fluxes within a single station approach 2,500 dpm m^{-2} d^{-1} at 125 m, with a few reaching 3,000 dpm m^{-2} d^{-1} or higher by 200 m (**Figure 2** and Table S1). In contrast, some of the lowest fluxes overlapped with zero at 200 m. At greater depths, there is more variability as SS fluxes continued to increase at some stations, while other SS fluxes decreased more sharply due to a greater ^{234}Th excess below 80–100 m.

While the assumption of SS essentially suggests that no change in ^{234}Th flux occurred over the 28-day sampling period, the SS model can also be used to infer fluxes prior to sampling, depending on the response time of the radionuclide. For ^{234}Th, the SS response time in a given water parcel is shorter than its mean life with respect to decay ($1/^{234}\lambda = 35$ days) due to scavenging by sinking particles ($1/k$, where k is first-order removal rate; Turnewitsch et al., 2008). Here, k was calculated from the removal flux, that is, the rate of scavenging onto sinking particles divided by the total ^{234}Th inventory. Using the upper 50 m ^{234}Th inventory as an example (**Table 1**), k was calculated to be on the order of approximately 0.02 d^{-1}, and thus the total response time for ^{234}Th was approximately 20 days (residence time of total $^{234}\text{Th} = 1/[^{234}\lambda + k]$). We therefore consider the calculated SS fluxes to also represent the average flux over the 3 weeks prior to the start of sampling.

4.3.2. Physical processes versus non-steady-state model

Water column ^{234}Th activities within the upper 60 m increased a small but significant amount between Epochs 1 and 3 (**Figure 3** and Figure S1), either due to a temporal weakening in particulate export and/or to the transport of waters with higher ^{234}Th activities into the sampling area from below (upwelling/eddy turbulent mixing) or from horizontal advection and diffusion. We examined each component separately, as the data did not allow for both temporal (non-steady-state, NSS) and physical processes to be resolved using Equation 1.

4.3.3. Non-steady-state model

Non-steady-state model As sampling occurred following a Lagrangian framework, the increase in ^{234}Th activity during the field campaign was most likely due to temporal variability associated with changes in biological processes (see Section 5.1). If we assume that the increase in ^{234}Th activity during the cruise was only due to NSS processes, we can solve Equation 1 and assume that $\frac{d(^{234}Th)}{dt}$ equals the change in ^{234}Th activity observed between epochs:

$$\text{NSS} = \int_{z=D}^{0} \lambda \times \frac{\left(1 - e^{-\lambda \Delta t}\right)^{238}\text{U} + {}^{234}\text{Th}_{e1} e^{-\lambda \Delta t} - {}^{234}\text{Th}_{e3}}{1 - e^{-\lambda \Delta t}}, \quad (4)$$

where the average ^{234}Th activity of Epochs 1 and 3 are $^{234}\text{Th}_{e1}$ and $^{234}\text{Th}_{e3}$, respectively, and Δt is the time between the midpoints of Epochs 1 and 3 (18 days).

Downloaded from http://online.ucpress.edu/elementa/article-pdf/8/1/030/468942/elementa.2020.030.pdf by guest on 11 July 2024

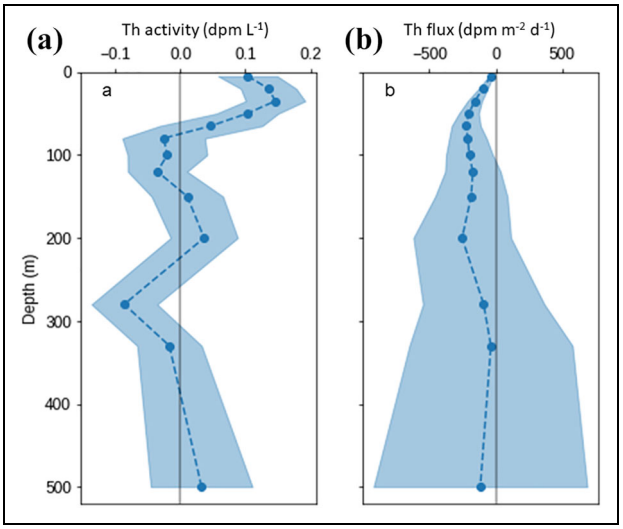

Figure 3. Temporal changes in ^{234}Th activity. Mean difference between Epoch 3 and Epoch 1 (E3–E1). (a) Thorium activity (dpm L^{-1}) and (b) steady-state thorium flux (dpm m^{-2} d^{-1}) versus depth. Shading shows the standard error of the difference in means. DOI: https://doi.org/10.1525/elementa.2020.030.f3

The choice of using Epochs 1 and 3 (and excluding Epoch 2) was motivated by two limitations of the NSS model. First, the NSS model is valid only if the same water mass is sampled over time (Savoye et al., 2006), and if the measurements capture temporal changes in ^{234}Th activity in a Lagrangian framework versus a spatial gradient (Resplandy et al., 2012). Second, the uncertainty on the NSS model is relatively high due to error propagation, such that on timescales < 10 days, the errors are too large to be meaningful (Savoye et al., 2006). Epochs 1 and 3 were sampled 18 days apart and covered a small spatial area (approximately 35 km × 35 km) following a central Lagrangian float. These sampling periods therefore provided the best conditions for application of the NSS model (Resplandy et al., 2012). In contrast, Epoch 2 was a survey designed to capture larger spatial gradients (approximately 88 km × 88 km) that took place within 10 days of both Epochs 1 and 3.

To compute the NSS model, ^{234}Th activity measurements were averaged by depth bin for Epochs 1 and 3. Each depth bin included 12–41 ^{234}Th measurements per epoch, with the exception of the 280 m depth bin, which was on average more sparsely sampled (**Table 1**). NSS integrated export flux at each depth *D* was then calculated according to Equation 4. The uncertainty on the NSS flux estimate includes the standard deviation of ^{234}Th activity measurements in each depth bin per epoch propagated through Equation 4. The NSS models yield export estimates that are approximately 30% lower than the SS model in the upper 60 m and persist throughout the water column as this lower flux is propagated to deeper depths (**Table 1** and **Figure 3b**).

4.3.4. Consideration of physical transport

Consideration of physical transport If we assume that the increase in ^{234}Th activity during the cruise was only due to physical processes, we can evaluate the influence of the physical transport term, *V*, as follows:

$$V = u\frac{\partial^{234}\mathrm{Th}}{\partial x} + v\frac{\partial^{234}\mathrm{Th}}{\partial y} + w\frac{\partial^{234}\mathrm{Th}}{\partial z} + \frac{\partial k\partial^{234}\mathrm{Th}}{\partial z^2}, \quad (5)$$

where *u*, *v*, *w*, and $\frac{d(^{234}Th)}{dx}, \frac{d(^{234}Th)}{dy}, \frac{d(^{234}Th)}{dz}$ are the zonal, meridional, and vertical components of the velocity and the thorium gradient, and *k* is the vertical eddy diffusivity coefficient. The first three terms represent horizontal and vertical advection while the last term represents the effect of vertical eddy turbulent mixing.

The vertical transport was estimated using measured vertical ^{234}Th gradients, vertical velocity, and eddy diffusivity estimated at Station P from 2 years of Seaglider data by Pelland et al. (2017). Vertical velocity, *w*, is largely associated with seasonal Ekman pumping and was equal to 0.25 m d^{-1} at the time of the cruise. Vertical diffusivity, *k*, decreased with depth from 10^{-3} m^2 s^{-1} above the transition layer (<35 m), to 10^{-4} m^2 s^{-1} within the transition layer (35–80 m), to 10^{-5} m^2 s^{-1} at depths >80 m. Together vertical advection and vertical eddy mixing supplied less than 20 dpm m^{-2} d^{-1} in the upper 25 m and influenced ^{234}Th export by <6% in all epochs (Figure S2).

The horizontal transport was estimated at a scale of 50–100 km, where we had both ^{234}Th activity gradients and horizontal velocities of 2–3 km d^{-1}, mostly to the northeast, derived from acoustic Doppler current profiler measurements in the upper 25 m of the mixed layer (Siegel et al., 2020). Thorium-234 activities varied on scales <10 km during the survey (Figure S3), indicating the presence of small-scale spatio-temporal variations that were not considered in the transport estimates. Here, we used the average difference in ^{234}Th between Epochs 1 and 3 (1.36 dpm L^{-1} versus 1.48 dpm L^{-1} in the upper 25 m, the shallowest 2 depth bins in **Table 1**) and a maximum horizontal velocity of 3 km d^{-1} (0.035 m s^{-1}) across the distance of the sampling patch (75 km) to calculate a horizontal gradient of 1.6 × 10^{-6} dpm L^{-1} m^{-1} along the direction of the northeastward flow. This yielded a maximum horizontal input term of 0.005 dpm L^{-1} d^{-1} or 125 dpm m^{-2} d^{-1}. This is less than 20% of the ^{234}Th export derived from radioactive production and decay using the SS model (666 dpm m^{-2} d^{-1} in upper 25 m, **Table 1**), decreasing in importance with depth due to a reduction in current velocities.

Combined, the above results suggest that along the Lagrangian trajectory of the float, horizontal and vertical transport added at most 145 dpm m^{-2} d^{-1} of ^{234}Th between Epochs 1 and 3 in the upper 25 m, with the magnitude relative to the total ^{234}Th flux decreasing with increasing depth. In other words, transport terms can reduce ^{234}Th fluxes in the surface by about 20% due to the input of higher ^{234}Th activity waters from below or transported horizontally. The SS model with physical transport is qualitatively consistent with ^{234}Th fluxes but would have a smaller impact on them than if calculated by the NSS model. As noted above, we cannot separate NSS from

Downloaded from http://online.ucpress.edu/elementa/article-pdf/8/1/030/468942/elementa.2020.030.pdf by guest on 11 July 2024

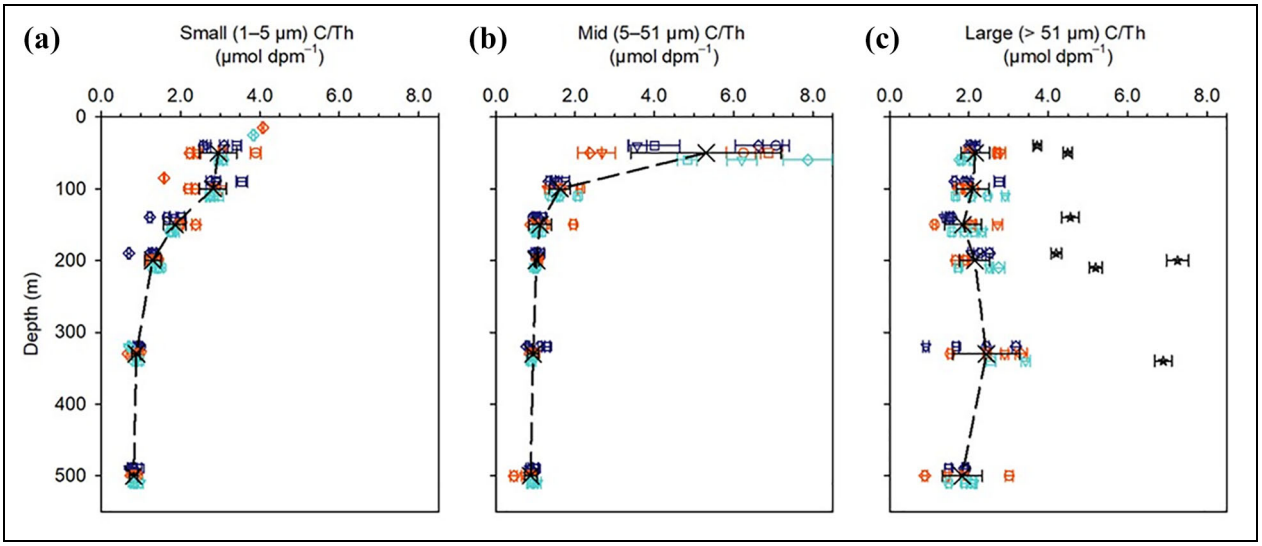

Figure 4. POC/^{234}Th ratio profile for different size class particles. POC/^{234}Th ratios (C/Th) in (a) small (1–5 µm), (b) mid (5–51 µm), and (c) large (>51 µm) particles collected during the EXPORTS cruise at Ocean Station Papa on 12 in situ pump casts (4/Epoch: Epoch 1 = dark blue; Epoch 2 = red; Epoch 3 = turquoise). Data from each epoch have been spaced out by 10 m to facilitate visualization. Symbols show different stations (see metadata at https://seabass.gsfc.nasa.gov/archive/WHOI/buesseler/EXPORTS/EXPORTSNP/archive/). Black crosses show the arithmetic mean (± standard deviation) of C/Th ratios at the depths where in situ pumps were deployed (50, 100, 150, 200, 330, and 500 m ± 5 m), and the dashed lines show C/Th values interpolated linearly (see Section 4.4). Additional data ($n = 5$) of small particles collected at 20, 85, and 320 m in Epochs 2 and 3 are shown on the left panel. C/Th outliers for large particles are shown by stars on the right panel. EXPORTS = EXport Processes in the Ocean from RemoTe Sensing; POC = particulate organic carbon. DOI: https://doi.org/10.1525/elementa.2020.030.f4

physical transport processes; therefore, we chose to consider 2 end-member models, that is, the SS model without transport (high end-member) and the NSS model (low end-member).

Importantly, the difference between the 2 end-member models (referred to as SS and NSS in the text) becomes indistinguishable within uncertainties at depth (**Table 1**). Given the error estimates in applying SS versus NSS models and the assumptions inherent in the modeling exercise, we used the average of both models to determine a best estimate of POC flux during the entire cruise, propagating the error of both models on the average ^{234}Th-derived POC flux at a given depth horizon (see Section 4.5).

4.4. Particulate C/^{234}Th ratios

To estimate the flux of POC from ^{234}Th, one must use the C/Th ratio associated with sinking particles. Generally, C/Th ratios are more variable in shallow waters, decrease with depth, and are similar among large size class particles and those found in sediment traps (Buesseler et al., 2006). There are some exceptions, attributed most often to C-rich "swimmers" in the largest particles (Buesseler et al., 2007; Liu et al., 2009). Here we present data from the size-fractionated particles separated via filters and screens into >1–5 µm (small), 5–51 µm (mid), and > 51 µm (large) size classes (**Figure 4**). No significant temporal changes in C/Th were observed. As such, we focus the remainder of this section on changes in the C/Th ratios across all epochs with increasing depth and with differing size class. Results are summarized in **Table 2**.

Average C/Th ratios in all size-fractionated particles were determined from the arithmetic mean (± standard deviation) at each sampled depth. C/Th ratios determined from the slopes of linear relationships between POC concentrations and ^{234}Th activities produced comparable results (Table S2). Here, we focus on depth-specific arithmetic means to enable consistency across particle size classes. C/Th ratios at 65, 80, 120, and 280 m were interpolated linearly between sample depths (shown in italics, **Table 2**).

For small particles, C/Th ratios averaged 2.82–2.95 µmol dpm^{-1} at 50–100 m and decreased to 0.82–0.89 µmol dpm^{-1} by 330–500 m (**Table 2**). Two samples collected within the mixed layer at 20 m (**Figure 4a**) showed C/Th ratios a factor of 1.3 higher (3.95 ± 0.17 µmol dpm^{-1}) than that measured below the mixed layer at 50–100 m.

For mid-sized particles, the average C/Th ratios at 50 m, 5.3 ± 1.9 µmol dpm^{-1}, were almost double those measured in the small particles at the same depth, yet decreased sharply to 1.12–0.88 µmol dpm^{-1} by 150–500 m (**Table 2** and **Figure 5**). The highest variability occurred in the upper 50 m (**Figure 4b**), consistent with enhanced primary production in the Ez.

Large particles showed similar C/Th ratios with depth (**Figure 4c**), ranging from 1.83 to 2.44 µmol dpm^{-1} excluding 7 outliers (see Section 3.2). We hypothesize that the lack of a decrease in C/Th ratio with increasing depth is likely due to the presence of zooplankton contamination. While nondetrital zooplankton identified by the naked eye were picked from the 51-µm screens,

Downloaded from http://online.ucpress.edu/elementa/article-pdf/8/1/030/468942/elementa.2020.030.pdf by guest on 11 July 2024

Table 2. Cruise-average POC/^{234}Th ratios. DOI: https://doi.org/10.1525/elementa.2020.030.t2

Depth (m)	POC/^{234}Th (μmol dpm^{-1})[a]					
	1–5 μm		5–51 μm		>51 μm[b]	
	Average	*SD*	Average	*SD*	Average	*SD*
50	2.95	0.47	5.30	1.90	2.16	0.36
65	*2.91*	*0.43*	*4.20*	*1.26*	*2.14*	*0.38*
80	*2.87*	*0.39*	*3.09*	*0.75*	*2.12*	*0.39*
100	2.82	0.34	1.62	0.26	2.09	0.41
120	*2.44*	*0.32*	*1.41*	*0.28*	*2.00*	*0.44*
150	1.85	0.28	1.12	0.29	1.85	0.47
200	1.30	0.21	1.03	0.06	2.15	0.38
280	*1.03*	*0.14*	*0.97*	*0.12*	*2.32*	*0.65*
330	0.89	0.10	0.94	0.15	2.44	0.84
500	0.82	0.10	0.88	0.16	1.83	0.51

POC = particulate organic carbon.

[a]POC/^{234}Th (C/Th) ratios for size-fractionated particles were measured at 50, 100, 150, 200, 330, and 500 m. Average C/Th at these depths were obtained from the arithmetic mean (± standard deviation, *SD*). Values shown in italics are linearly interpolated (see Section 4.4).

[b]Seven >51 μm samples (of 72) were identified as outliers due to swimmer contamination (see Section 3.2) and therefore are excluded from the average.

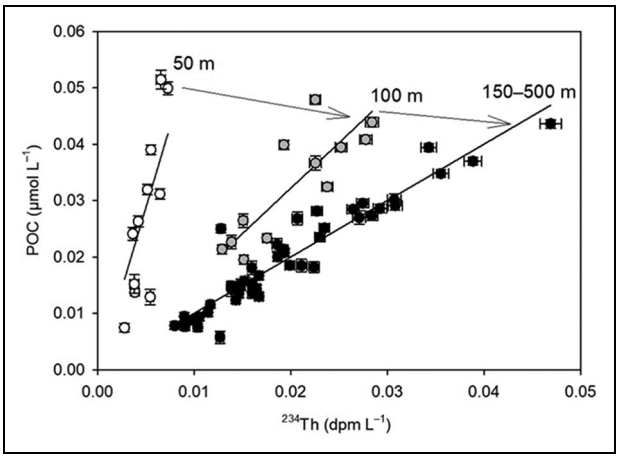

Figure 5. Relationship between particulate organic carbon (POC) and ^{234}Th. POC (μmol L^{-1}) vs. ^{234}Th (dpm L^{-1}) linear relationships at different depths in mid (5–51 μm) particles combining 12 in situ pump casts. White dots show data from 50 m, gray dots from 100 m, and black dots from 150, 200, 330, and 500 m. Error bars indicate standard deviation of the mean (n = 12). DOI: https://doi.org/10.1525/elementa.2020.030.f5

subsequent photographic analysis of the samples indicated the possible presence of nonpicked swimmers in about 20–30 samples, although only 7 of these samples had statistically higher C/Th ratios (**Figure 4c**; discussion at end of Section 3.2).

In most prior studies, C/Th ratios decrease with depth due to the preferential heterotrophic utilization of C as a food source (e.g., see reviews by Buesseler et al., 2006; Puigcorbé et al., 2020). The high and invariant C/Th ratio with depth in the >51 μm pump samples suggests pervasive contamination by zooplankton swimmers. During the EXPORTS campaign, individual samples were collected on the process ship using zooplankton nets (D Steinberg and her EXPORTS team). Both large and small pteropods were characterized by C/Th ratios of approximately 24, radiolarians approximately 44, and up to 825 μmol dpm^{-1} for small amphipods (data not shown). We estimate that the presence of just 1 amphipod or 2 radiolarians in a given sample could have increased the C/Th ratio by a factor of 2. This estimate supports our hypothesis of swimmer contributions resulting in higher C/Th in >51 μm filtered samples. Therefore, we consider the large size class as an unreliable indicator of the C/Th ratio of passively sinking particles.

4.5. POC flux profiles

With a known C/Th ratio versus depth, the POC flux can be calculated at any depth and location where ^{234}Th fluxes are available. This conversion to C flux fails only if the C/Th ratio used differs from the flux-weighted C/Th ratio representative of sinking particles. Given the similarity across all epochs in C/Th ratios for a given size class, especially at depths below 50 m (**Figure 4**), depth-specific mean C/Th ratios were used to estimate POC flux. As such, station-by-station differences in POC flux were driven by variations in ^{234}Th flux.

We determined a best estimate of POC flux using the average of the POC fluxes calculated from the SS and NSS models and using C/Th from the mid-sized particles (**Table 3**). Overall, this average cruise estimate showed a POC flux peak of 5.5 ± 1.7 mmol C m^{-2} d^{-1} at 50 m. This depth was above the 1% PAR and thus represented a layer where POC was likely still being produced by autotrophs (**Figure 6**). Note that there is no mid-sized C/Th data above 50 m, and hence, the 50 m ratio can be used to roughly estimate the POC flux at shallower depths where ^{234}Th results were available. However, as a result, POC fluxes at depths shallower than 50 m might be underestimated, and they were certainly less well constrained. There was a sharp decline in the average POC fluxes below the 50 m POC flux maximum to approximately 1.7 mmol C m^{-2} d^{-1} at the 0.1% PAR and PPZ depths (120 m). Below these deeper Ez boundaries, there was only a modest decrease in POC fluxes to between 1.1 and 1.3 mmol C m^{-2} d^{-1} (**Table 3**).

We note that the C/Th ratio of mid-sized particles collected using in situ pumps was assumed to be most representative of the population of sinking particles. However, for completeness, we also include POC fluxes derived using the C/Th ratios measured in other size classes and using both SS and NSS ^{234}Th flux models (Table S3). For example, the use of C/Th ratios measured in small-sized particles resulted in a smaller decline in POC flux with depth, with a POC flux maximum at 100 m of 3.5 mmol C m^{-2} d^{-1} that decreased to 3.0 mmol C m^{-2} d^{-1}

Downloaded from http://online.ucpress.edu/elementa/article-pdf/8/1/030/468942/elementa.2020.030.pdf by guest on 11 July 2024

Table 3. Cruise-average POC fluxes. DOI: https://doi.org/10.1525/elementa.2020.030.t3

	POC Flux SS (mmol C m^{-2} d^{-1})[a]		POC Flux NSS (mmol C m^{-2} d^{-1})[b]		Average POC Flux (mmol C m^{-2} d^{-1})[c]	
	5–51 μm		5–51 μm		5–51 μm	
Depth (m)	Average	Uncert	Average	Uncert	Average	Uncert
50	6.77	2.65	4.19	2.22	5.48	1.73
65	5.91	2.07	3.81	1.98	4.86	1.43
80	4.47	1.38	3.08	1.63	3.77	1.07
100	2.35	0.62	1.66	0.92	2.01	0.56
120	2.02	0.66	1.45	0.99	1.74	0.60
150	1.55	0.62	1.05	1.00	1.30	0.59
200	1.32	0.61	0.80	1.30	1.06	0.72
280	1.15	0.45	1.06	1.34	1.11	0.71
330	1.38	0.86	1.19	1.85	1.28	1.02
500	1.34	1.01	0.98	2.14	1.16	1.19

Abbreviations: POC = particulate organic carbon; Uncert = uncertainties.

[a]POC fluxes were calculated by multiplying the C/Th ratio in 5–51 μm particles (2) by the cruise-average steady-state (SS) ^{234}Th flux (**Table 1**) at a given depth; uncertainties, by propagating the C/Th ratio and ^{234}Th flux uncertainties.

[b]POC fluxes were calculated by multiplying the C/Th ratio in 5–51 μm particles (**Table 2**) by the non-steady-state (NSS) ^{234}Th flux (**Table 1**) at a given depth; uncertainties, by propagating the C/Th ratio and ^{234}Th flux uncertainties.

[c]Average POC flux was calculated by averaging the SS and NSS POC flux estimates using the C/Th ratio in 5–51 μm particles; uncertainties, by propagating the uncertainties of the SS and NSS POC flux estimates.

by the PPZ (120 m bin). POC fluxes from 200 to 500 m converge to 1.1–1.3 mmol C m^{-2} d^{-1}, the same as those calculated using the mid-sized particles. Using the large-particle C/Th ratio resulted in calculated POC fluxes from 50 to 500 m that ranged from 2.1 to 3.3 mmol C m^{-2} d^{-1} with no discernible depth patterns.

5. Discussion

5.1. POC flux estimates during EXPORTS at Ocean Station Papa

The POC flux derived from our extensive ^{234}Th survey, using C/Th ratios in mid-sized particles and the average of SS and NSS ^{234}Th models, was 5.5 mmol C m^{-2} d^{-1} at 50 m decreasing to 1.7 mmol C m^{-2} d^{-1} by 120 m (**Figure 6** and **Table 3**), which was near the depth of the PPZ (117 ± 5 m) and $Ez_{0.1}$ (118 ± 9 m). While individual ^{234}Th depth profiles varied, the calculated differences in the spatial distributions of POC fluxes at 120 m throughout the EXPORTS study area were relatively small (**Figure 7**). These results were consistent with spatially coherent temperature and salinity measurements that indicate similar water masses were sampled during the cruise (Figure S4). In contrast, the increase in ^{234}Th activity by Epoch 3, consistent with a decline in particle fluxes, aligned with a temporal increase in chlorophyll concentrations (**Figure 1**) that is consistent with a decrease in C export. Spatially, while ^{234}Th flux profiles showed considerable similarity with increasing depth (**Figure 2**), closer examination of individual flux profiles showed that relatively distinct differences still existed, with some stations showing a greater decrease with depth (a larger ^{234}Th excess) and others continuing to increase or remain constant below the upper 80–120 m. These results imply that processes below the Ez, or the characteristics of the particles exiting the Ez, such as their lability and sinking rates, were variable and led to differing degrees of POC flux attenuation (see Figure S5 for spatial maps of POC flux at 50, 100, 150, and 200 m).

Sinking particle fluxes were also measured during the EXPORTS campaign using surface-tethered traps and neutrally buoyant sediment traps deployed for 3–5 days per epoch at 5 depths spanning from 100 to 500 m (Estapa et al., 2020). Similar to the largest size fraction, and consistent with many prior sediment trap studies, swimmers increased the measured POC flux in the traps. Large amounts of swimmer C were removed using a 335-μm screen and manual picking under a microscope, though some small swimmers were likely to have passed through the mesh. In the trap samples, this additional swimmer contribution to POC flux was estimated statistically through comparison to mass, ^{234}Th and biogenic silica fluxes, and removed from the trap fluxes reported here (Estapa et al., 2020). The swimmer-corrected sediment trap POC fluxes ranged from 0.45 to 2.8 mmol C m^{-2} d^{-1} from 100 to 200 m, lower than ^{234}Th-derived POC fluxes (regardless of C/Th size class) at the same depths (Figure S6 and Table S3). Unlike ^{234}Th-derived estimates, sediment trap POC fluxes were characterized by an increase in POC flux in Epoch 3 relative to Epochs 1 and 2 (from 0.9 to 2.3 mmol C m^{-2} d^{-1} at 100 m). This

Downloaded from http://online.ucpress.edu/elementa/article-pdf/8/1/030/468942/elementa.2020.030.pdf by guest on 11 July 2024

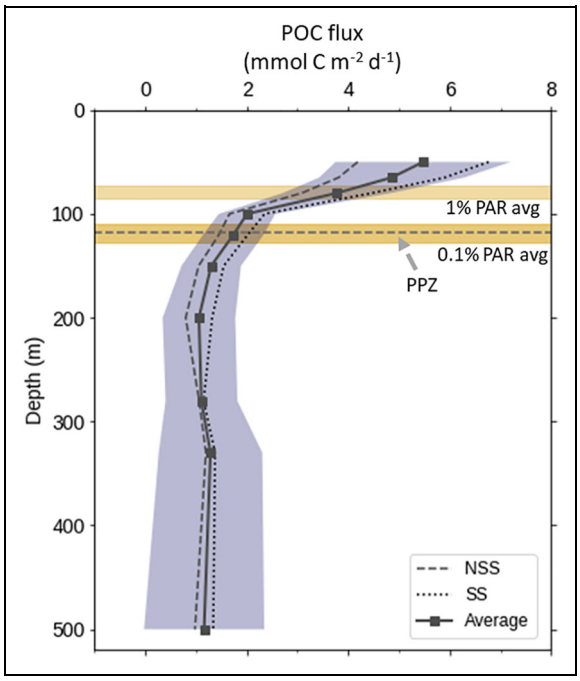

Figure 6. Cruise-average particulate organic carbon (POC) flux. Best estimate of cruise-average POC flux (mmol C m^{-2} d^{-1}) versus depth (solid line, square markers) from the average of the steady-state (SS, dotted) and non-steady-state (NSS, dashed) 1-dimensional models. Shading indicates the propagated uncertainties of the SS and NSS POC flux estimates. Yellow bars are the cruise-average 1% photosynthetic active radiation (PAR) and 0.1% PAR regions. Dashed horizontal line is the bottom of the primary production zone (PPZ). DOI: https://doi.org/10.1525/elementa.2020.030.f6

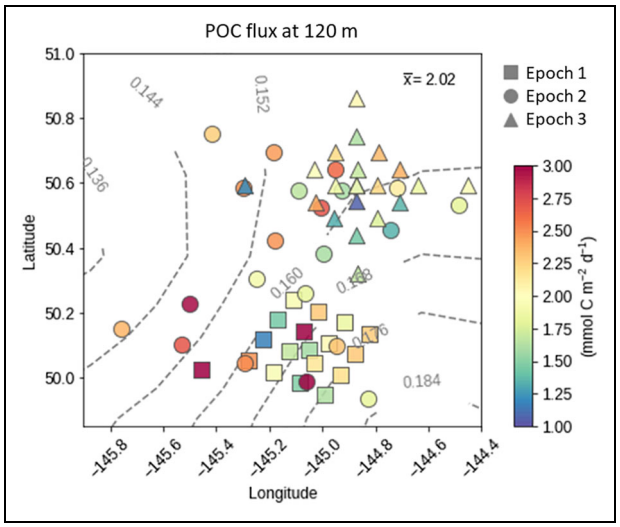

Figure 7. Particulate organic carbon (POC) flux at 120 m. Station map of steady-state POC flux (mmol C m^{-2} d^{-1}, colors) in the 120 m depth bin. Shape denotes epoch. Contours are sea surface height anomaly (m) from AVISO, averaged over the duration of cruise. DOI: https://doi.org/10.1525/elementa.2020.030.f7

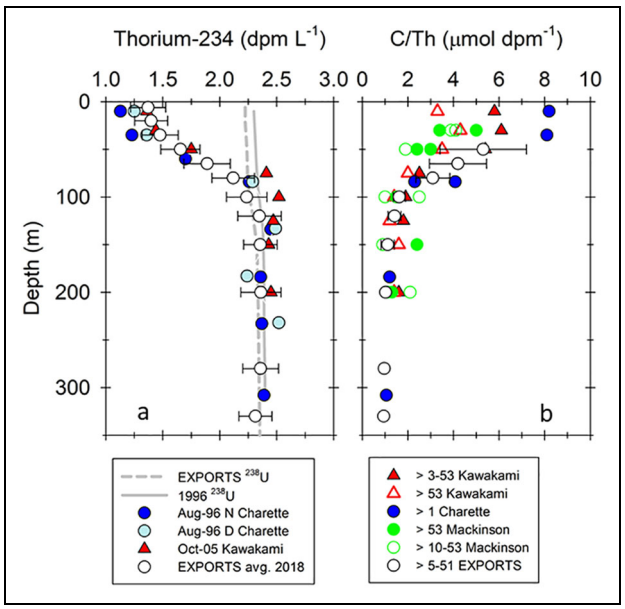

Figure 8. Historical ^{234}Th studies at Ocean Station Papa. (a) Historical ^{234}Th activities (dpm L^{-1}) from Charette et al. (1999; blue circles) and Kawakami et al. (2010; red triangles) are compared to EXPORTS average (white circles with standard deviation, n = 41–114 samples per depth interval). Vertical dashed line shows ^{238}U as determined in this study; solid line, as reported in Charette et al. (1999). (b) C/Th ratios (µmol dpm^{-1}) from those same studies plus Mackinson et al. (2015) for filtered particle size classes as indicated. DOI: https://doi.org/10.1525/elementa.2020.030.f8

increase in the traps and decrease in the ^{234}Th-derived POC fluxes (i.e., increase in ^{234}Th activities) may be due to the temporal differences in the integration times of the 2 methods (3–5 days for traps versus 3 weeks for ^{234}Th). The higher Epoch 3 trap flux is more similar to our best estimate of the ^{234}Th-derived POC fluxes at 100 m. A more detailed consideration of trap fluxes and a comparison to water column-derived ^{234}Th fluxes will be presented in the study of Estapa et al. (2020).

5.2. Prior studies of POC flux at Ocean Station Papa

A few previous studies have examined ^{234}Th-derived POC fluxes at Station P. Charette et al. (1999) collected ^{234}Th profiles in February, May, and twice in August 1996 along the Canadian "Line P" repeat sampling program that transects from the British Columbian coast to Station P. Their ^{234}Th activities at Station P in August overlap with our data more than 25 years later (**Figure 8a**); their fluxes of 1,500 dpm m^{-2} d^{-1} at approximately 200 m are similar to those measured at the same depths during EXPORTS using a similar SS model (1,300 $\pm$ 600 dpm m^{-2} d^{-1}). This coherence is particularly notable, given that Charette et al. (1999) used a slightly different method. A large volume pumping system was used to scavenge dissolved ^{234}Th onto Mn impregnated cartridges, and particulate ^{234}Th was collected using a 1-µm cartridge filter, though POC was measured on a separate quartz filter, identical to the 1 µm QMA used in this study. Despite these different

Downloaded from http://online.ucpress.edu/elementa/article-pdf/8/1/030/468942/elementa.2020.030.pdf by guest on 11 July 2024

Table 4. Comparison of POC fluxes at Ocean Station Papa. DOI: https://doi.org/10.1525/elementa.2020.030.t4

	POC Export Flux (mmol C m^{-2} d^{-1}) by Depth				
Data Source	**50 m**	**100 m**	**200 m**	**500 m**	**Comments**
^{234}Th-based					
This study	5.5 ± 1.7	2.01 ± 0.56	1.06 ± 0.72	1.16 ± 1.19	Aug–Sept, avg. of 61 profiles; >5–51 μm C/Th (Table 3)
Charette et al. (1999)	8.1 ± 3.4[a]	—[b]	—[b]	—[b]	August single profile; >1 μm C/Th
Kawakami et al. (2010)	—[b]	2.3 ± 0.5	—[b]	—[b]	October, single profile; >0.7 μm C/Th
Mackinson et al. (2015)	4.1 ± 0.6	3.0 ± 0.1	2.0 ± 0.8	—[b]	June 2011 and 2012; recalculated here from 3 profiles; >53 μm C/Th
Trap-based					
Wong et al. (2002)	10.4 ± 3.1	3.9 ± 2.5	4.0 ± 1.2	1.9 ± 0.4	July–Sept avg.; includes unpublished data (F Whitney, M Robert, pers. comm.)
Timothy et al. (2013)	—[b]	—[b]	1.3	—[b]	Deep moored time-series traps, annual avg.
Estapa et al. (2020)	—[b]	1.38 ± 0.77	0.76 ± 0.24	0.86 ± 0.43	Aug–Sept EXPORTS cruise, avg. of 3 casts
Mackinson et al. (2015)	11.8 ± 1.7	6.2 ± 0.3	6.8 ±1.8	—[b]	June 2011 and 2012, avg. of 2 deployments, no poison

Abbreviations: Avg. = average; EXPORTS = EXport Processes in the Ocean from RemoTe Sensing; POC = particulate organic carbon.

[a]POC flux measured at 40 m which was considered to be the base of the $Ez_{0.1}$ (Charette et al., 1999).

[b]Indicates data not available.

techniques, their >1 μm C/Th data also overlap with our 5–51 μm size class and showed a clear decrease with depth down to 200–300 m, where C/Th ratios varied from 1.0 to 1.2 μmol dpm^{-1} (**Figure 8b**). Charette et al. (1999) reported the maximum POC flux of 8.1 mmol C m^{-2} d^{-1} at 40 m for their August sampling at Station P which is a bit higher but similar to our estimates (**Table 4**).

Kawakami et al. (2010) also measured ^{234}Th at Station P in October 2005. Again, they reported nearly identical ^{234}Th activities (**Figure 8a**), ^{234}Th fluxes, and the same low and decreasing C/Th ratios at depth (<2 μmol dpm^{-1}) in size-fractionated particulate samples collected with 3- and 53-μm size filters, similar to our EXPORTS results (**Figure 8b**). Finally, a more recent study at Station P includes ^{234}Th data and C/Th ratios from pumps in June for both 2011 and 2012 (Mackinson et al., 2015). Their data show good agreement as well for both ^{234}Th (^{234}Th fluxes within 25% of EXPORTS in upper 200 m) and similar C/Th ratios on their >10–53 μm and >53 μm filers (**Figure 8b**). All of these studies reported a decrease in C/Th with depth, which supports our use of the 5–51 μm C/Th ratios in this study. This broad agreement over 25 years of ^{234}Th fluxes and C/Th ratios suggests that similar conditions were sampled at Station P.

In addition to ^{234}Th measurements, sediment trap work has been pursued at Station P for decades, most notably the deep-moored conical sediment trap time series at 3,800 m initiated by Wong in 1982 and ending in 2006 as summarized by Timothy et al. (2013). A second trap at 1,000 m was added in 1983, and a third trap at 200 m was added in 1989. There was a concern that the fluxes at the shallower 200 m depth were too low due to low trap collection efficiencies, as evidenced, for example, in that study by an increase in biogenic silica flux with depth. Overall lower trapping efficiencies are common for moored traps at depths shallower than 1,500 m based upon ^{230}Th and ^{231}Pa budgets (Scholten et al., 2001; Yu et al., 2001; Buesseler et al., 2007). Timothy et al. (2013) reported an annual average POC flux of 1.3 mmol C m^{-2} d^{-1} at 200 m (**Table 4**), very similar to what we derived from ^{234}Th at 200 m, yet their POC fluxes were considered a lower limit due to their concerns that these fluxes were due to low trapping efficiencies, though they did not have ^{230}Th data to quantify this potential bias.

Perhaps more comparable to our ^{234}Th data are a series of shorter, 2-to 5-day deployments between 1987 and 1998 of drifting traps as summarized in the study of Wong et al. (2002) and augmented with additional data through 2004 (F Whitney and M Robert, pers. comm. 10/15/2019). These traps were modeled on the VERTEX cylindrical design (Knauer et al., 1979) and were deployed more than 20 times at up to 10 depths between 50 and 1,000 m, mostly during the spring and summer with a few deployments in autumn and winter. They reported a POC flux as high as 11.3 mmol C m^{-2} d^{-1} at 50 m in summer, which decreased rapidly to 6.1 mmol C m^{-2} d^{-1} at 100 m and 4.4 mmol C m^{-2} d^{-1} by 200 m. Those POC fluxes are higher than the EXPORTS fluxes, though the depth trend is similar (Figure S6). Closer examination of only their July to September deployments shows that average POC fluxes were similar to the annual means, with 10.4 ± 3.1 mmol C m^{-2} d^{-1} at the 50 m maximum and 4.0 ± 1.2 mmol C

Downloaded from http://online.ucpress.edu/elementa/article-pdf/8/1/030/468942/elementa.2020.030.pdf by guest on 11 July 2024

m^{-2} d^{-1} by 200 m (**Table 4** and Figure S6). Given our concerns with swimmer removal using 335-µm screens (Estapa et al., 2020), we hypothesize that one possible cause for the higher drifting sediment trap POC fluxes is that small swimmers were not removed by either the 500- or 1,000-µm screens that Wong et al. (2002) used to separate swimmers from passively sinking trap material. Additional evidence for swimmer contamination noted by Wong et al. (2002) is the high C/N ratio and a positive intercept of C versus N (positive C flux when N is zero).

While Mackinson et al. (2015) also used similar 3-day drifting traps as in the study of Wong et al. (2002), they did not poison their traps, which is not recommended (Buesseler et al., 2007). Their C flux results were higher than the other trap studies, for example, by a factor of 4–9 below 100 m compared to Estapa et al. (2020; **Table 4**). Whether the higher fluxes are due to the lack of poison, or perhaps higher flux conditions during the June bloom versus late summer period, is difficult to know. However, their trap fluxes are also higher than their own ^{234}Th-derived C fluxes by a factor of 2–3 (**Table 4**).

A number of global assessments of POC flux using ^{234}Th have been made (Le Moigne et al., 2013; Henson et al., 2019). Le Moigne et al. (2013) examined ^{234}Th-derived POC fluxes at 100–150 m and noted that their global patterns and magnitudes were similar to those predicted in global models (Laws et al., 2000; Schlitzer, 2004). However, they cautioned that there were considerable data gaps in high export and high productivity settings, particularly in regions dominated by upwelling. Mean POC fluxes averaged 9 mmol C m^{-2} d^{-1}, albeit across a huge range, from approximately 0 to >100 mmol C m^{-2} d^{-1}. Within the biogeochemical Longhurst province that includes Station P (East Pacific Subarctic Gyre), POC fluxes averaged 4.1 $\pm$ 2.6 mmol C m^{-2} d^{-1}, about double our results at these depths, although the compilation of Le Moigne et al. (2013) also included locations closer to the coast. Overall, our finding of a POC flux maximum during EXPORTS of 5.5 mmol C m^{-2} d^{-1} at 50 m, decreasing to a flux of 1–2 mmol C m^{-2} d^{-1} at the base of the Ez and below, places the Station P site as one of the more modest C flux settings.

5.3. Biological carbon pump efficiencies at Ocean Station Papa

Marine ecosystems regulate the global biogeochemical cycling of C through the uptake of inorganic C via photosynthesis and the transformation of this C into a variety of organic forms that are transported to depth via sinking particles, although additional export of organic materials can occur through a variety of other physical and biogeochemical processes as well (Boyd et al., 2019). Here, we tracked the net export of POC using ^{234}Th and quantified the strength of the biological pump and the efficiency of sinking POC transport through the upper twilight zone where most of the remineralization occurs (Buesseler et al., 2020). Combined, these processes determine the overall efficiency of the biological C pump (BCP).

One of the simplest measures of the strength of the BCP is export efficiency or the ratio of export production (EP) to NPP. When EP is determined by sediment traps, it is often referred to as the e-ratio (Murray et al., 1989). When derived using the ^{234}Th approach, as done here, EP is defined as the ThE ratio (Buesseler et al., 1998). Regardless of the method, the depth over which the EP comparison is made is critical, given the rapid changes in the BCP with increasing depth. Buesseler and Boyd (2009) suggested that an Ez-normalized depth is most appropriate for examining the BCP efficiencies because below the Ez, POC losses dominate as the formation of new POC via photosynthesis cannot occur. Defining the depth of the Ez by light or PAR sensors, however, does not work at night and is influenced by time of day and local variations in cloud cover. In contrast, sensors for fluorescence are more common and are not impacted by these issues. As such, using fluorescence as a real-time indicator of Ez is often a more practical way to define the PPZ. As introduced by Owens et al. (2015), the PPZ is defined as the depth where in situ fluorescence declines to 10% of the maximum signal measured in overlying waters. During EXPORTS, the depths of 0.1% PAR ($Ez_{0.1}$), the PPZ, and where ^{234}Th reaches equilibrium with ^{238}U overlapped at 100–125 m (**Figure 1**). The depth of the $Ez_{0.1}$ during EXPORTS can thus be estimated using the PPZ.

During EXPORTS, the average Ez ratio (POC flux/NPP) was 13% $\pm$ 5% when using the best estimate of POC fluxes at 120 m ($Ez_{0.1}$) and average integrated NPP determined from ^{14}C methods using onboard incubations (the average of 11 profiles collected throughout the cruise is 13 $\pm$ 2 mmol C m^{-2} d^{-1}; J Fox, pers. comm. 1/18/2020; ^{14}C data available at https://seabass.gsfc.nasa.gov/archive/OSU/behrenfeld/EXPORTS/EXPORTSNP/archive). We reemphasize the strong dependence of the Ez ratio on the chosen POC flux depth. Here, Ez ratios increased to 29% if assessed at 80 m or at the average depth of $Ez_{1.0}$. As noted above, the ^{234}Th results and C/Th ratios measured during EXPORTS are similar to the much earlier data presented in Charette et al. (1999). However, Charette et al. also reported much higher rates of NPP, 58 and 85 mmol C m^{-2} d^{-1} in May and August, respectively, which results in somewhat lower estimates of the Ez ratio of 3% and 14% (for May and Aug, respectively; Buesseler and Boyd, 2009). Likewise using the ^{234}Th-derived C flux estimates and a higher NPP in June (50–105 mmol C m^{-2} d^{-1}) resulted in lower Ez ratios of 3%–6% ($Ez_{1.0}$) in the study by Mackinson et al. (2015) conducted in June (**Table 3** in Mackinson et al., 2015).

To assess POC flux attenuation below Ez, we quantified a transfer efficiency, or T_{100}, which is defined as the ratio of the POC flux 100 m below the Ez to the POC flux at the base of the Ez (using PPZ or 0.1% PAR; Buesseler and Boyd, 2009). Using the average POC flux, T_{100} averages 61% using the 120- and 220-m POC fluxes (220-m flux is approximated from the estimated POC flux at 200 m; **Table 3**). In other words, about 40% of the POC flux is remineralized in the upper 100 m of the twilight zone. If we used the POC flux peak at 50 m (5.5 mmol C m^{-2} d^{-1}), T_{100} would be significantly lower (24%). As stated earlier, the Ez ratio at Station P (14%) reported by Charette et al. (1999) was similar to EXPORTS in August; however, their

Downloaded from http://online.ucpress.edu/elementa/article-pdf/8/1/030/468942/elementa.2020.030.pdf by guest on 11 July 2024

POC flux attenuation was higher, with a T_{100} around 30% (70% lost). Although their normalization depth and local $Ez_{0.1}$ were reported to be at 40 m during their August sampling, in hindsight, the phytoplankton dynamics at Station P (Boyd and Harrison, 1999) suggest that their $Ez_{0.1}$ was likely much deeper. In effect, their higher POC attenuation reflects a shallower portion of the POC flux profiles and thus an enhanced attenuation bias, as discussed in the study of Buesseler et al. (2020). Mackinson et al. (2015) reported an $Ez_{1.0}$ depth of 60–85 m in June; extrapolating their average ^{234}Th-derived C fluxes to 75 and 175 m (from **Table 4**) resulted in a T_{100} closer to 80% or less POC flux attenuation in June.

During EXPORTS, sediment traps show a similar gradient in POC flux below $Ez_{0.1}$ as determined using ^{234}Th, although the ^{234}Th-derived gradient was steeper above the shallowest trap flux assessment at 100 m (Figure S6; Estapa et al., 2020). The trap fluxes would result in a cruise-averaged Ez ratio of 10 $\pm$ 6% at a nominal 100-m depth (i.e., bracketed by $Ez_{1.0}$ and $Ez_{0.1}$), and a T_{100} of 55 $\pm$ 35% between the nominal 100- and 200-m trap depths (Estapa et al., 2020). These results are in good agreement with the ^{234}Th-derived POC fluxes presented here. Earlier Station P moored trap data (Timothy et al., 2013) resulted in an EP/NPP ratio of only 3% at 200 m; however, this ratio is derived from an average NPP of 40 mmol C m^{-2} d^{-1}; hence, the export ratio is lower due to higher NPP, not lower fluxes. These moored time-series flux data were most useful for observing annual patterns of export. Climatologies of the 200- and 1,000-m Station P sediment trap time-series presented in the study of Timothy et al. (2013) suggest that the August to September time frame is one of the strongly decreasing fluxes, especially at 200 m. The trend toward higher ^{234}Th activities in Epoch 3 during EXPORTS may therefore reflect a seasonal shift. Interestingly, they noted that by the time the sinking particles reached 3,800 m, POC fluxes were 1.6 times higher than the average measured in deep moored traps in the Sargasso Sea. Timothy et al. (2013) attributed the higher deepwater fluxes to higher biogenic silica and carbonate contents of Station P fluxes that facilitated more efficient transport, at least deeper in the water column. These higher BCP efficiencies were not observed in EXPORTS in the upper twilight zone.

Globally, the Ez ratio varies from a few percentage to >50% (Buesseler and Boyd, 2009; Buesseler et al., 2020). Thus, an Ez ratio of 13% (from ^{234}Th) was on the lower end but not as low as some oligotrophic settings. With this Ez ratio and T_{100} around 61%, the BCP at Station P is relatively inefficient, with only 8% of the organic carbon fixed in the Ez, reaching a depth of 100 m below the Ez. This overall efficiency was slightly higher than that calculated from data of Charette et al. (1999) for conditions at Station P in August (4%) and similar to what has been found in a reassessment of BCP during late bloom conditions in the northwest Pacific during VERTIGO and in summer conditions at the UK Porcupine Abyssal Plain site in the northeast Atlantic (Buesseler et al., 2020). Low overall BCP efficiencies in the summer and late summer in these comparable settings are seasonal in nature. For example, there is much higher export during spring bloom conditions in the northeast Atlantic, where the overall BCP efficiency can approach 50% during the demise of the local diatom spring bloom.

The overall BCP efficiencies here are similar to, or a bit higher than, those measured in the subtropical gyre time-series sites, Station ALOHA (A Long-Term Oligotrophic Habitat Assessment; 5% using ^{234}Th; Buesseler and Boyd, 2009) and Bermuda Atlantic Time-series Study (BATS; 1%–5% using traps; Buesseler et al., 2020). At these sites, both the ^{234}Th fluxes and C/Th ratios were low. Interestingly at Station P, the late summer average ^{234}Th flux (1,230 dpm m^{-2} d^{-1} at 120 m) was higher than average ^{234}Th fluxes at Station ALOHA (annual average = 765 dpm m^{-2} d^{-1} from 1999 to 2000; Benitez-Nelson et al., 2001a) and BATS (annual average = 600 dpm m^{-2} d^{-1} for 1993–1995; Sweeney et al., 2003). Lower C/Th ratios at Station P during EXPORTS, however, resulted in a low POC flux, given the higher relative ^{234}Th flux. Low particulate C/Th ratios are hypothesized to be due to some combination of efficient recycling of organic matter and/or smaller particle sizes (Buesseler et al., 2006). In contrast, the higher C/Th ratios (>10 μmol dpm^{-1}) typical of the Southern Ocean and phytoplankton blooms are often associated with larger diatoms species and high POC export (Buesseler et al., 2001, 2006; Puigcorbé et al., 2020). These larger size classes of plankton were not dominant at Station P during EXPORTS, nor are they common at other sites with low BCP efficiencies (Puigcorbé et al., 2015). The conditions encountered during EXPORTS were similar to what Henson et al. (2019) referred to as a low NPP (<85 mmol C m^{-2} d^{-1}) and moderate export efficiency regime (EP/NPP 2%–20% at 100 m). These regimes are characterized by ecosystems with small primary producers that are tightly coupled to recycling by zooplankton and bacteria. They are also characteristic of subpolar waters such as Station P and many sites in the oligotrophic and equatorial open ocean of the Atlantic.

6. Conclusions

We have used an extensive set of ^{234}Th measurements to quantify the spatial (horizontal scales of <10 km and vertical scales of tens of meters) and temporal (days to weeks) variability in export fluxes associated with sinking particles and their flux attenuation below the Ez. Our best estimate of the maximum flux of POC, using C/Th ratios measured on 5–51 μm particles and both SS and NSS models, was 5.5 mmol C m^{-2} d^{-1} at 50 m, decreasing rapidly with depth within the euphotic zone. This attenuation resulted in < 2 mmol C m^{-2} d^{-1} reaching the depth of the $Ez_{0.1}$, which was near the base of the PPZ (117 m), where the PPZ defined the transition between shallower autotrophic production of particulate organic matter and the twilight zone where heterotrophic and physical processes reduce POC fluxes. Changes with time and space were small, although a statistically significant increase in ^{234}Th activities during the sampling period was observed in the upper 60 m. When compared to NPP, average export efficiencies were relatively low (13%) and characteristic of a modest biological carbon pump. Interestingly, these

Downloaded from http://online.ucpress.edu/elementa/article-pdf/8/1/030/468942/elementa.2020.030.pdf by guest on 11 July 2024

latest results agreed with prior ^{234}Th studies within the past 25 years at Station P, suggesting similar conditions for BCP efficiencies in the late summer at this site.

These results are the first comprehensive assessment of POC flux from the first EXPORTS campaign and provide a foundation for comparisons with future efforts that focus on the larger suite of EXPORTS measurements that were made during the study, including spatial variability in plankton community structure, particle size and composition, and other biological and physical processes. In addition, the downward flux of other elements and compounds, including particulate nitrogen, biogenic silica, phosphorus, and inorganic C, will be calculated for comparison to POC, using their ratios to ^{234}Th on pump-collected samples and other estimates of net community production. Combined, these results will allow the development of mechanistic and predictive models of POC flux and the inclusion of other C loss terms associated with physical mixing transporting nonsinking POC and DOM to depth, and POC loss associated with the diel and seasonal vertical migrations of zooplankton (e.g., Boyd et al., 2019). These models are of critical importance if we are to better understand and predict the influence of marine ecosystems on the storage, transformation, and fate of carbon and associated elements in the Earth's biosphere.

Data Accessibility Statement

Buesseler, KO, Benitez-Nelson, CR, Resplandy, L, Clevenger, S, Drysdale, J, Pike, S, Roca-Martí, M, Umhau, B, Wyatt, A (2019) EXPORTS-EXPORTSNP_thorium_234_survey, SeaBASS repository, DOI: 10.5067/SeaBASS/EXPORTS/DATA001, https://seabass.gsfc.nasa.gov/archive/WHOI/buesseler/EXPORTS/EXPORTSNP/archive/

Buesseler, KO, Benitez-Nelson, CR, Resplandy, L, Roca-Martí, M, Pike, S, Umhau, B, Horner, T, Masqué, P (2019) EXPORTS-EXPORTSNP_IN_SITU_PUMPS_SURVEY, SeaBASS repository, DOI: 10.5067/SeaBASS/EXPORTS/DATA001, https://seabass.gsfc.nasa.gov/archive/WHOI/buesseler/EXPORTS/EXPORTSNP/archive/

Estapa, M, Buesseler, KO, Omand, M, Durkin, C (2019) EXPORTS-EXPORTSNP_flux-POC_NBST, EXPORTS-EXPORTSNP_flux-POC_STT, EXPORTS-EXPORTSNP_flux-Th_234_NBST, EXPORTS-EXPORTSNP_flux-Th_234_STT, SeaBASS repository, DOI: 10.5067/SeaBASS/EXPORTS/DATA001, https://seabass.gsfc.nasa.gov/archive/SKIDMORE/estapa/EXPORTS/EXPORTSNP/archive

Supplemental files

The supplemental files for this article can be as follows:

- **Text S1.** Figures S1-S6. Tables S1-S3. PDF.

Acknowledgments

EXPORTS would not have been possible without the conceptual and organizational leadership of Dave Siegel and the many participants in the planning process. On these cruises, we are gratefully appreciative of the captain and crew of the R/V *Sally Ride* and scientists on board as well as other EXPORTS scientists and support from the R/V *Roger Revelle*. We also want to thank James Fox, Michael Behrenfeld, and their group for providing the ^{14}C primary production data; Debbie Steinberg and her group for providing samples of plankton from the nets; Colleen Durkin, Melissa Omand, Alyson Santoro, and Pat Kelly for their contributions to the sediment trapping program; and the Canadian scientists who conducted the prior trap studies at Ocean Station Papa, including Frank Whitney and Marie Robert, who provided results for our consideration of the drifting trap fluxes beyond which had been published previously. Finally, we thank the editors of *Elementa* for their efforts and for finding two very constructive reviewers whose comments helped greatly in improving the revised manuscript.

Author contributions

Contributed to conception and design: KOB, CBN, and LR.

Contributed to acquisition of data: KOB, CBN, MRM, AMW, SJC, JD, SP, MLE, and BPU.

Contributed to analysis and interpretation of data: KOB, CBN, MRM, AMW, LR, and MLE.

Drafted and/or revised the article: KOB, CBN, MRM, AMW, LR, SJC, MLE, and BPU.

Approved the submitted version for publication: KOB, CBN, MRM, AMW, LR, SJC, JD, MLE, SP, and BPU.

Funding

The authors would like to acknowledge support from the National Aeronautics and Space Administration (NASA) as part of the EXport Processes in the Ocean from RemoTe Sensing (EXPORTS) program awards 80NSSC17K0555 and 80NSSC17K0662; the Woods Hole Oceanographic Institution's Ocean Twilight Zone study for KOB and MRM, and the National Science Foundation Graduate Research Fellowship Program (NSF-GRFP) for funding and support of AW.

References

Beaugrand, G, Edwards, M, Legendre, L. 2010. Marine biodiversity, ecosystem functioning, and carbon cycles. *Proc Natl Acad Sci USA* **107**(22): 10120–10124.

Benitez-Nelson, CR, Buesseler, KO, Karl, DM, Andrews, J. 2001a. A time-series study of particulate matter export in the North Pacific Subtropical Gyre based on 234Th: 238U disequilibrium. *Deep Sea Res Part I* **48**(12): 2595–2611.

Benitez-Nelson, CR, Buesseler, KO, Rutgers Van Der Loeff, MM, Andrews, J, Ball, L, Crossin, G, Charette, MA. 2001b. Testing a new small-volume technique for determining 234Th in seawater. *J Radioanal Nucl Chem* **248**(3): 795–799. DOI: https://doi.org/10.1023/A:1010621618652.

Benitez-Nelson, CR, McGillicuddy, DJ. 2008. Mesoscale physical–biological–biogeochemical linkages in the open ocean: An introduction to the results of the E-Flux and EDDIES programs. *Deep Sea Res Part II* **55**: 1133–1138.

Bif, MB, Hansell, DA. 2019. Seasonality of dissolved organic carbon in the upper Northeast Pacific Ocean. *Global Biogeochem Cycles* **33**(5): 526–539.

Downloaded from http://online.ucpress.edu/elementa/article-pdf/8/1/030/468942/elementa.2020.030.pdf by guest on 11 July 2024

Boyd, P, Harrison, P. 1999. Phytoplankton dynamics in the NE subarctic Pacific. *Deep Sea Res Part II* **46**(11–12): 2405–2432.

Boyd, PW, Claustre, H, Levy, M, Siegel, DA, Weber, T. 2019. Multi-faceted particle pumps drive carbon sequestration in the ocean. *Nature* **568**(7752): 327–335.

Buesseler, K, Ball, L, Andrews, J, Benitez-Nelson, C, Belastock, R, Chai, F, Chao, Y. 1998. Upper ocean export of particulate organic carbon in the Arabian Sea derived from thorium-234. *Deep Sea Res Part II* **45**(10): 2461–2487. DOI: https://doi.org/10.1016/S0967-0645(98)80022-2.

Buesseler, KO, Antia, AN, Chen, M, Fowler, SW, Gardner, WD, Gustafsson, O, Harada, K, Michaels, AF, Rutgers Van Der Loeff, MM, Sarin, M, Steinberg, DK, Trull, T. 2007. An assessment of the use of sediment traps for estimating upper ocean particle fluxes. *J Mar Res* **65**(3): 345–416.

Buesseler, KO, Bacon, MP, Cochran, JK, Livingston, HD. 1992. Carbon and nitrogen export during the JGOFS North Atlantic bloom experiment estimated from 234Th:238U disequilibria. *Deep Sea Res* **39**(7/8): 1115–1137.

Buesseler, KO, Ball, L, Andrews, J, Cochran, JK, Hirschberg, DJ, Bacon, MP, Fleer, A, Brzezinski, M. 2001. Upper ocean export of particulate organic carbon and biogenic silica in the Southern Ocean along 170 W. *Deep Sea Res Part II* **48**(19–20): 4275–4297.

Buesseler, KO, Benitez-Nelson, CR, Moran, S, Burd, A, Charette, M, Cochran, JK, Coppola, L, Fisher, NS, Fowler, SW, Gardner, WD, Guo, LD, Gustafsson, Ö, Lamborg, C, Masque, P, Miquel, JC, Passow, U, Santschi, PH, Savoye, N, Stewart, G, Trull, T. 2006. An assessment of particulate organic carbon to thorium-234 ratios in the ocean and their impact on the application of 234Th as a POC flux proxy. *Mar Chem* **100**(3–4): 213–233.

Buesseler, KO, Boyd, PW. 2009. Shedding light on processes that control particle export and flux attenuation in the twilight zone of the open ocean. *Limnol Oceanogr* **54**(4): 1210–1232.

Buesseler, KO, Boyd, PW, Black, EE, Siegel, DA. 2020. Metrics that matter for assessing the ocean biological carbon pump. *Proc Natl Acad Sci USA* **117**(18): 9679–9687.

Burd, AB, Hansell, DA, Steinberg, DK, Anderson, TR, Arístegui, J, Baltar, F, Beaupré, SR, Buesseler, KO, DeHairs, F, Jackson, GA, Kadko, DC, Koppelmann, R, Lampitt, RS, Nagata, T, Reinthaler, T, Robinson, C, Robison, BH, Tamburini, C, Tanaka, T. 2010. Assessing the apparent imbalance between geochemical and biochemical indicators of meso- and bathypelagic biological activity: What the@ $#! is wrong with present calculations of carbon budgets? *Deep Sea Res Part II* **57**(16): 1557–1571.

Charette, MA, Moran, SB, Bishop, JK. 1999. 234Th as a tracer of particulate organic carbon export in the subarctic northeast Pacific Ocean. *Deep Sea Res Part II* **46**(11–12): 2833–2861.

Chavez, FP, Messié, M, Pennington, JT. 2011. Marine primary production in relation to climate variability and change. *Annu Rev Mar Sci* **3**: 227–260.

Cutter, GA, Casciotti, K, Croot, P, Geibert, W, Heimbürger, L-E, Lohan, M, Planquette, H, van de Flierdt, T. 2017. Sampling and sample-handling protocols for GEOTRACES Cruises, Version 3.0. DOI: http://dx.doi.org/10.25607/OBP-2.

Doney, SC, Ruckelshaus, M, Duffy, JE, Barry, JP, Chan, F, English, CA, Galindo, HM, Grebmeier, JM, Hollowed, AB, Knowlton, N, Polovina, J, Rabalais, NN, Sydeman, WJ, Talley, LD. 2012. Climate change impacts on marine ecosystems. *Ann Rev Mar Sci* **4**: 11–37.

Estapa, ML, Buesseler, K, Durkin, CA, Omand, M, Benitez-Nelson, CR, Roca-Martí, M, Breves, E, Kelly, RP, Pike, S. 2020. Biogenic sinking particle fluxes at Ocean Station Papa. *Elementa Science of the Anthropocene*. Manuscript submitted for publication.

Estapa, ML, Siegel, D, Buesseler, K, Stanley, R, Lomas, M, Nelson, NB. 2015. Decoupling of net community and export production on submesoscales in the Sargasso Sea. *Global Biogeochem Cycles* **29**(8): 1266–1282.

Falkowski, P, Scholes, R, Boyle, E, Canadell, J, Canfield, D, Elser, J, Gruber, N, Hibbard, K, Högberg, P, Linder, S, Mackenzie, FT, Moore III, B, Pedersen, T, Rosenthal, Y, Seitzinger, S, Smetacek, V, Steffen, W. 2000. The global carbon cycle: A test of our knowledge of earth as a system. *Science* **290**(5490): 291–296.

Fassbender, AJ, Sabine, CL, Feifel, KM. 2016. Consideration of coastal carbonate chemistry in understanding biological calcification. *Geophys Res Lett* **43**(9): 4467–4476. DOI: 10.1002/2016gl068860.

Gustafsson, Ö, Gschwend, PM, Buesseler, KO. 1997. Using 234Th disequilibria to estimate the vertical removal rates of polycyclic aromatic hydrocarbons from the surface ocean. *Mar Chem* **57**(1–2): 11–23.

Hamme, RC, Nicholson, DP, Jenkins, WJ, Emerson, SR. 2019. Using noble gases to assess the ocean's carbon pumps. *Annu Rev Mar Sci* **11**: 75–103.

Haskell II, WZ, Kadko, D, Hammond, DE, Knapp, AN, Prokopenko, MG, Berelson, W, Capone, DG. 2015. Upwelling velocity and eddy diffusivity from 7Be measurements used to compare vertical nutrient flux to export POC flux in the Eastern Tropical South Pacific. *Mar Chem* **168**: 140–150.

Henson, S, Le Moigne, F, Giering, S. 2019. Drivers of carbon export efficiency in the global ocean. *Global Biogeochem Cycles* **33**(7): 891–903.

Honjo, S, Dymond, J, Collier, R, Manganini, SJ. 1995. Export production of particles to the interior of the equatorial Pacific Ocean during the 1992 EqPac experiment. *Deep Sea Res Part II* **42**(2): 831–870.

Kawakami, H, Honda, MC, Matsumoto, K, Fujiki, T, Watanabe, S. 2010. East-west distribution of POC fluxes estimated from 234 Th in the northern North Pacific in autumn. *J Oceanogr* **66**(1): 71–83.

Downloaded from http://online.ucpress.edu/elementa/article-pdf/8/1/030/468942/elementa.2020.030.pdf by guest on 11 July 2024

Knauer, GA, Martin, JH, Bruland, KW. 1979. Fluxes of particulate carbon, nitrogen, and phosphorus in the upper water column of the northeast Pacific. *Deep Sea Res Part A* **26**(1): 97–108.

Kwon, EY, Primeau, F, Sarmiento, JL. 2009. The impact of remineralization depth on the air–sea carbon balance. *Nat Geosci* **2**(9): 630–635.

Lam, PJ, Ohnemus, DC, Auro, ME. 2015. Size-fractionated major particle composition and concentrations from the US GEOTRACES North Atlantic Zonal Transect. *Deep Sea Res Part II* **116**: 303–320.

Lamborg, C, Buesseler, K, Lam, P. 2008. Sinking fluxes of minor and trace elements in the North Pacific Ocean measured during the VERTIGO program. *Deep Sea Res Part II* **55**(14–15): 1564–1577.

Laws, EA, Falkowski, PG, Smith Jr, WO, Ducklow, H, McCarthy, JJ. 2000. Temperature effects on export production in the open ocean. *Global Biogeochem Cycles* **14**(4): 1231–1246.

Le Moigne, FA, Henson, S, Sanders, R, Madsen, E. 2013. Global database of surface ocean particulate organic carbon export fluxes diagnosed from the ^{234}Th technique. *Earth Syst Sci Data* **5**(2): 295–304.

Liu, Z, Cochran, JK, Lee, C, Gasser, B, Miquel, JC, Wakeham, SG. 2009. Further investigations on why POC concentrations differ in samples collected by Niskin bottle and in situ pump. *Deep Sea Res Part II* **56**(18): 1558–1567.

Mackinson, B, Moran, S, Lomas, M, Stewart, GM, Kelly, R. 2015. Estimates of micro-, nano-, and picoplankton contributions to particle export in the northeast Pacific. *Biogeosciences* **12**: 3429–3446.

Maiti, K, Buesseler, KO, Pike, SM, Benitez-Nelson, C, Cai, P, Chen, W, Cochran, K, Dai, M, Dehairs, F, Gasser, B, Kelly, RP, Masque, P, Miller, LA, Miquel, JC, Moran, SB, Morris, PJ, Peine, F, Planchon, F, Renfro, AA, Rutgers Van Der Loeff, MM, Santschi, PH, Turnewitsch, R, Waples, JT, Xu, C. 2012. Intercalibration studies of short-lived thorium-234 in the water column and marine particles. *Limnol Oceanogr Methods* **10**(9): 631–644.

McDonnell, AM, Lam, PJ, Lamborg, CH, Buesseler, KO, Sanders, R, Riley, JS, Marsay, C, Smith, HEK, Sargent, EC, Lampitt, RS, Bishop, JKB. 2015. The oceanographic toolbox for the collection of sinking and suspended marine particles. *Prog Oceanogr* **133**: 17–31.

Murray, JW, Downs, JN, Strom, S, Wei, C-L, Jannasch, HW. 1989. Nutrient assimilation, export production and 234Th scavenging in the eastern equatorial Pacific. *Deep Sea Res Part A* **36**(10): 1471–1489.

Owens, S, Buesseler, K, Sims, K. 2011. Re-evaluating the 238U-salinity relationship in seawater: Implications for the 238U–234Th disequilibrium method. *Mar Chem* **127**(1–4): 31–39.

Owens, SA, Pike, S, Buesseler, KO. 2015. Thorium-234 as a tracer of particle dynamics and upper ocean export in the Atlantic Ocean. *Deep Sea Res Part II* **116**: 42–59. DOI: https://doi.org/10.1016/j.dsr2.2014.11.010.

Pelland, NA, Eriksen, CC, Cronin, MF. 2017. Seaglider surveys at Ocean Station Papa: Diagnosis of upper-ocean heat and salt balances using least squares with inequality constraints. *J Geophys Res Oceans* **122**(6): 5140–5168.

Pike, S, Buesseler, K, Andrews, J, Savoye, N. 2005. Quantification of 234Th recovery in small volume sea water samples by inductively coupled plasma-mass spectrometry. *J Radioanal Nucl Chem* **263**(2): 355–360.

Puigcorbé, V, Benitez-Nelson, C, Masque, P, Verdeny, E, White, AE, Popp, BN, Prahl, FG, Lam, PJ. 2015. Small phytoplankton drive high summertime carbon and nutrient export in the Gulf of California and Eastern Tropical North Pacific. *Global Biogeochem Cycles* **29**(8). DOI: https://doi.org/10.1002/2015GB005134.

Puigcorbé, V, Masqué, P, Le Moigne, FA. 2020. Global database of ratios of particulate organic carbon to thorium-234 in the ocean: Improving estimates of the biological carbon pump. *Earth Syst Sci Data* **12**(2): 1267–1285.

Resplandy, L, Martin, A, Le Moigne, F, Martin, P, Aquilina, A, Mémery, L, Lévy, L, Sanders, R. 2012. How does dynamical spatial variability impact 234Th-derived estimates of organic export? *Deep Sea Res Part I* 68: 24–45.

Sarmiento, JL, Gruber, N. 2002. Sinks for anthropogenic carbon. *Physics Today* **55**(8): 30–36.

Savoye, N, Benitez-Nelson, C, Burd, AB, Cochran, JK, Charette, M, Buesseler, KO, Jackson, GA, Roy-Barman, M, Schmidt, S, Elskens, M. 2006. 234Th sorption and export models in the water column: A review. *Mar Chem* **100**(3–4): 234–249.

Schlitzer, R. 2004. Export production in the equatorial and North Pacific derived from dissolved oxygen, nutrient and carbon data. *J Oceanogr* **60**(1): 53–62.

Scholten, J, Fietzke, J, Vogler, S, Rutgers Van Der Loeff, MM, Mangini, A, Koeve, W, Waniek, J, Stoffers, P, Antia, A, Kuss, J. 2001. Trapping efficiencies of sediment traps from the deep Eastern North Atlantic: the 230Th calibration. *Deep Sea Res Part II* **48**(10): 2383–2408.

Shine, JP, Ika, RV, Ford, TE. 1995. Multivariate statistical examination of spatial and temporal patterns of heavy metal contamination in New Bedford Harbor marine sediments. *Environ Sci Technol* **29**(7): 1781–1788.

Siegel, DA, Buesseler, K, Behrenfeld, M, Benitez-Nelson, C, Boss, E, Brzezinski, MA, et al. 2020. Overview of the EXport Processes in the Ocean from RemoTe Sensing (EXPORTS) Northeast Pacific field deployment. *Elementa Science of the Anthropoene*, Manuscript submitted for publication.

Siegel, DA, Buesseler, KO, Behrenfeld, MJ, Benitez-Nelson, CR, Boss, E, Brzezinski, MA, Burd, A, Carlson, CA, D'Asaro, EA, Doney, SC, Perry, MJ, Stanley, RHR, Steinberg, DK. 2016. Prediction of the export and fate of global ocean net primary production: The EXPORTS science plan. *Front Mar Sci* **3**: 22.

Downloaded from http://online.ucpress.edu/elementa/article-pdf/8/1/030/468942/elementa.2020.030.pdf by guest on 11 July 2024

Stukel, MR, Aluwihare, LI, Barbeau, KA, Chekalyuk, AM, Goericke, R, Miller, AJ, Ohman, MD, Ruacho, A, Song, H, Stephens, BM, Landry, MR. 2017. Mesoscale ocean fronts enhance carbon export due to gravitational sinking and subduction. *Proc Natl Acad Sci USA* **114**(6): 1252–1257.

Sweeney, EN, McGillicuddy Jr, DJ, Buesseler, KO. 2003. Biogeochemical impacts due to mesoscale eddy activity in the Sargasso Sea as measured at the Bermuda Atlantic Time-series Study (BATS). *Deep Sea Res Part II* **50**(22–26): 3017–3039.

Timothy, D, Wong, C, Barwell-Clarke, J, Page, J, White, L, Macdonald, RW. 2013. Climatology of sediment flux and composition in the subarctic Northeast Pacific Ocean with biogeochemical implications. *Prog Oceanogr* **116**: 95–129.

Tukey, JW. 1977. *Exploratory data analysis*. Addison-Wesley, Reading, MA.

Turnewitsch, R, Reyss, J-L, Nycander, J, Waniek, JJ, Lampitt, RS. 2008. Internal tides and sediment dynamics in the deep sea—Evidence from radioactive 234Th/238U disequilibria. *Deep Sea Res Part I* **55**(12): 1727–1747.

Verdeny, E, Masqué, P, Garcia-Orellana, J, Hanfland, C, Cochran, JK, Stewart, GM. 2009. POC export from ocean surface waters by means of 234Th/238U and 210Po/210Pb disequilibria: A review of the use of two radiotracer pairs. *Deep Sea Res Part II* **56**(18): 1502–1518.

?**Wong, C, Waser, N, Whitney, F, Johnson, W, Page, J**. 2002. Time-series study of the biogeochemistry of the North East subarctic Pacific: reconciliation of the Corg/N remineralization and uptake ratios with the Redfield ratios. *Deep Sea Res Part II* **49**(24–25): 5717–5738.

Xie, RC, Le Moigne, FA, Rapp, I, Lüdke, J, Gasser, B, Dengler, M, Liebetrau, V, Achterberg, EP. 2020. Effects of 238U variability and physical transport on water column 234Th downward fluxes in the coastal upwelling system off Peru. *Biogeosciences Discussions*. DOI: https://doi.org/10.5194/bg-2020-57.

Yu, E-F, Francois, R, Bacon, M, Honjo, S, Fleer, A, Manganini, SJ, Rutgers Van Der Loeff, MM, Ittekot, V. 2001. Trapping efficiency of bottom-tethered sediment traps estimated from the intercepted fluxes of 230Th and 231 Pa. *Deep Sea Res Part I* **48**(3): 865–889.

Downloaded from http://online.ucpress.edu/elementa/article-pdf/8/1/030/468942/elementa.2020.030.pdf by guest on 11 July 2024

How to cite this article: Buesseler, KO, Benitez-Nelson, CR, Roca-Martí, M, Wyatt, AM, Resplandy, L, Clevenger, SJ, Drysdale, JA, Estapa, ML, Pike, S, Umhau, BP. 2020. High-resolution spatial and temporal measurements of particulate organic carbon flux using thorium-234 in the northeast Pacific Ocean during the EXport Processes in the Ocean from RemoTe Sensing field campaign. *Elem Sci Anth*. 8: 1. DOI: https://doi.org/10.1525/elementa.2020.030.

Domain Editor-in-Chief: Jody W. Deming, University of Washington, WA, USA

Guest Editor: Deborah Steinberg, Virginia Institute of Marine Science, William & Mary, Williamsburg, United States

Knowledge Domain: Ocean Science

Part of an Elementa Special Feature: EXPORTS

Published: December 10, 2020 **Accepted:** September 14, 2020 **Submitted:** March 13, 2020

Copyright: © 2020 The Author(s). This is an open-access article distributed under the terms of the Creative Commons Attribution 4.0 International License (CC-BY 4.0), which permits unrestricted use, distribution, and reproduction in any medium, provided the original author and source are credited. See http://creativecommons.org/licenses/by/4.0/.

ELEMENTA Science of the Anthropocene

Elem Sci Anth is a peer-reviewed open access journal published by University of California Press.

OPEN ACCESS